

Little red dot variability over a century reveals black hole envelope via a giant Einstein cross

Zijian Zhang^{1,2}, Mingyu Li³, Masamune Oguri^{4,5}, Xiaojing Lin³, Kohei Inayoshi¹, Catherine Cerny⁶, Dan Coe^{7,8,9}, Jose M. Diego¹⁰, Seiji Fujimoto^{11,12}, Linhua Jiang^{1,2,*}, Guillaume Mahler¹³, Jorryt Matthee¹⁴, Rohan P. Naidu¹⁵, Keren Sharon⁶, Yue Shen^{16,17}, Adi Zitrin¹⁸, Abdurro'uf¹⁹, Hollis Akins²⁰, Joseph F. V. Allingham¹⁸, Ricardo Amorín²¹, Yoshihisa Asada^{11,12}, Hakim Atek²², Franz E. Bauer²³, Maruša Bradač²⁴, Larry D. Bradley⁷, Zheng Cai³, Sebastiano Cantalupo²⁵, Christopher Conselice²⁶, Liang Dai²⁷, Pratika Dayal^{28,11,29}, Eiichi Egami³⁰, Daniel J. Eisenstein³¹, Andreas L. Faist³², Xiaohui Fan³⁰, Qinyue Fei¹¹, Brenda L. Frye³⁰, Yoshinobu Fudamoto⁴, Lukas J. Furtak^{20,33}, Miriam Golubchik¹⁸, Mauro González-Otero²¹, Yuichi Harikane³⁴, Tiger Yu-Yang Hsiao^{20,33}, Yolanda Jiménez-Teja^{21,35}, Jeyhan S. Kartaltepe³⁶, Tomokazu Kiyota^{37,38}, Anton M. Koekemoer⁷, Kotaro Kohno^{39,40}, Vasily Kokorev^{20,33}, Nimisha Kumari⁹, Ivo Labbe⁴¹, Claudia D. P. Lagos^{42,43}, Conor Larison⁷, Yongming Liang^{34,38}, Ray A. Lucas⁷, Jianwei Lyu³⁰, Nicholas S. Martis²⁴, Georgios E. Magdis^{43,44}, Matteo Messa⁴⁵, Minami Nakane^{34,46}, Gaël Noirot⁷, Rafael Ortiz III⁴⁷, Masami Ouchi^{38,34,37,48}, Justin D. R. Pierel⁷, Marc Postman⁷, Naveen Reddy⁴⁹, Massimo Ricotti⁵⁰, Daniel Schaerer^{51,52}, Raffaella Schneider⁵³, Charles C. Steidel⁵⁴, Wei Leong Tee⁵⁵, Roberta Tripodi^{56,24,57}, James A. A. Trussler³¹, Hiroya Umeda^{34,46}, Francesco Valentino^{43,44}, Eros Vanzella⁴⁵, Feige Wang⁶, Rogier Windhorst⁴⁷,

Yunjing Wu³, Zihao Wu³¹, Hiroto Yanagisawa^{34,46}, Jinyi Yang⁶, Fengwu Sun^{31,*}

¹Kavli Institute for Astronomy and Astrophysics, Peking University, Beijing 100871, China

²Department of Astronomy, School of Physics, Peking University, Beijing 100871, China

³Department of Astronomy, Tsinghua University, Beijing 100084, People's Republic of China

⁴Center for Frontier Science, Chiba University, 1-33 Yayoi-cho, Inage-ku, Chiba 263-8522, Japan

⁵Department of Physics, Graduate School of Science, Chiba University, 1-33 Yayoi-Cho, Inage-Ku, Chiba 263-8522, Japan

⁶Department of Astronomy, University of Michigan 1085 South University Avenue Ann Arbor, MI 48109, USA

⁷Space Telescope Science Institute (STScI), 3700 San Martin Drive, Baltimore, MD 21218, USA

⁸Center for Astrophysical Sciences, Department of Physics and Astronomy, The Johns Hopkins University, 3400 N Charles St. Baltimore, MD 21218, USA

⁹Association of Universities for Research in Astronomy (AURA), Inc. for the European Space Agency (ESA)

¹⁰Instituto de Física de Cantabria (CSIC-UC). Avda. Los Castros s/n. 39005 Santander, Spain

¹¹David A. Dunlap Department of Astronomy and Astrophysics, University of Toronto, 50 St. George Street, Toronto, Ontario, M5S 3J8, Canada

¹²Dunlap Institute for Astronomy and Astrophysics, 50 St. George Street, Toronto, Ontario, M5S 3H4, Canada

¹³STAR Institute, Quartier Agora - Allée du six Août, 19c B-4000 Liège, Belgium

¹⁴Institute of Science and Technology Austria (ISTA), Am Campus 1, 3400 Klosterneuburg, Austria

¹⁵MIT Kavli Institute for Astrophysics and Space Research, 70 Vassar Street, Cambridge, MA 02139, USA

¹⁶Department of Astronomy, University of Illinois Urbana-Champaign, Urbana, IL 61801, USA

¹⁷National Center for Supercomputing Applications, University of Illinois Urbana-Champaign, Urbana, IL 61801, USA

¹⁸Department of Physics, Ben-Gurion University of the Negev, P.O. Box 653, Beer-Sheva 8410501, Israel

¹⁹Department of Astronomy, Indiana University, 727 East Third Street, Bloomington, IN 47405, USA

²⁰Department of Astronomy, The University of Texas at Austin, 2515 Speedway Blvd Stop C1400, Austin, TX 78712, USA

²¹Instituto de Astrofísica de Andalucía (CSIC), Apartado 3004, 18080 Granada, Spain

²²Institut d'Astrophysique de Paris, CNRS, Sorbonne Université, 98bis Boulevard Arago, 75014, Paris, France

²³ Instituto de Alta Investigación, Universidad de Tarapacá, Casilla 7D, Arica, 1010000, Chile

- ²⁴University of Ljubljana FMF, Jadranska 19, 1000 Ljubljana, Slovenia
- ²⁵Dipartimento di Fisica G. Occhialini, Università degli Studi di Milano Bicocca, Piazza della Scienza 3, 20126 Milano, Italy
- ²⁶Jodrell Bank Centre for Astrophysics, University of Manchester, Oxford Road, Manchester UK
- ²⁷Department of Physics, University of California, 366 Physics North MC 7300, Berkeley, CA. 94720, USA
- ²⁸Canadian Institute for Theoretical Astrophysics, 60 St George St, University of Toronto, Toronto, ON M5S 3H8, Canada
- ²⁹Department of Physics, 60 St George St, University of Toronto, Toronto, ON M5S 3H8, Canada
- ³⁰Department of Astronomy/Steward Observatory, University of Arizona, 933 N. Cherry Ave, Tucson, AZ 85721, USA
- ³¹Center for Astrophysics | Harvard & Smithsonian, 60 Garden St., Cambridge, MA 02138, USA
- ³²IPAC, California Institute of Technology, 1200 E. California Blvd. Pasadena, CA 91125, USA
- ³³Cosmic Frontier Center, The University of Texas at Austin, Austin, TX 78712, USA
- ³⁴Institute for Cosmic Ray Research, The University of Tokyo, 5-1-5 Kashiwanoha, Kashiwa, Chiba 277-8582, Japan
- ³⁵Observatório Nacional, Rua General José Cristino, 77 - Bairro Imperial de São Cristóvão, Rio de Janeiro, 20921-400, Brazil
- ³⁶Laboratory for Multiwavelength Astrophysics, School of Physics and Astronomy, Rochester Institute of Technology, 84 Lomb Memorial
- ³⁷Department of Astronomical Science, The Graduate University for Advanced Studies, SOKENDAI, 2-21-1 Osawa, Mitaka, Tokyo, 181-8588, Japan
- ³⁸National Astronomical Observatory of Japan, 2-21-1 Osawa, Mitaka, Tokyo, 181-8588, Japan
- ³⁹Institute of Astronomy, Graduate School of Science, The University of Tokyo, 2-21-1 Osawa, Mitaka, Tokyo, 181-0015 Japan
- ⁴⁰Research Center for the Early Universe, Graduate School of Science, The University of Tokyo, 7-3-1 Hongo, Bunkyo-ku, Tokyo 113-0033, Japan
- ⁴¹Centre for Astrophysics and Supercomputing, Swinburne University of Technology, Melbourne, VIC 3122, Australia
- ⁴²International Centre for Radio Astronomy Research (ICRAR), M468, University of Western Australia, 35 Stirling Hwy, Crawley, WA 6001, Australia
- ⁴³Cosmic Dawn Center (DAWN), Jagtvej 128, DK2200 Copenhagen N, Denmark
- ⁴⁴DTU-Space, Technical University of Denmark, Elektrovej 327, 2800, Kgs. Lyngby, Denmark
- ⁴⁵INAF – OAS, Osservatorio di Astrofisica e Scienza dello Spazio di Bologna, via Gobetti 93/3, I-40129 Bologna, Italy
- ⁴⁶Department of Physics, Graduate School of Science, The University of Tokyo, 7-3-1 Hongo, Bunkyo, Tokyo 113-0033, Japan
- ⁴⁷School of Earth and Space Exploration, Arizona State University, Tempe, AZ 85287-6004, USA

⁴⁸Kavli Institute for the Physics and Mathematics of the Universe (WPI), The University of Tokyo, 5-1-5 Kashiwanoha, Kashiwa, Chiba, Japan

⁴⁹Department of Physics and Astronomy, University of California, Riverside, 900 University Avenue, Riverside, CA 92521, USA

⁵⁰Department of Astronomy, University of Maryland, College Park, 20742, USA

⁵¹Observatoire de Genève, Université de Genève, Chemin Pegasi 51, 1290 Versoix, Switzerland

⁵²CNRS, IRAP, 14 Avenue E. Belin, 31400 Toulouse, France

⁵³Department of Physics, Sapienza University of Rome, P.zza.le Aldo Moro 5, 00185 Rome, Italy

⁵⁴Cahill Center for Astronomy and Astrophysics, California Institute of Technology, MS 249-17, Pasadena, CA 91125

⁵⁵Department of Astronomy and Astrophysics, The Pennsylvania State University, 525 Davey Lab, University Park, PA 16802, USA

⁵⁶INAF - Osservatorio Astronomico di Roma, Via Frascati 33, I-00078 Monte Porzio Catone, Italy

⁵⁷IFPU - Institute for Fundamental Physics of the Universe, via Beirut 2, I-34151 Trieste, Italy

*Corresponding authors. Email: fengwu.sun@cfa.harvard.edu (Fengwu Sun) & jiangKIAA@pku.edu.cn (Linhua Jiang)

“Little red dots” (LRDs) represent a new population of astronomical objects uncovered by JWST whose nature remains debated. Although many LRDs are suspected as active galactic nuclei (AGN), they show little variability on days-years timescales. We report the discovery of two gravitationally lensed LRDs at redshift ~ 4.3 behind the cluster RXCJ2211-0350, one of which (RX1) is quadruply imaged with time delays spanning ~ 130 years. RX1 exhibits intrinsic color and brightness variations of up to 0.7 magnitude among its images. These changes are consistent with blackbody-temperature variations of a photosphere, indicating long-term variability analogous to Cepheid-like pulsations but in a far more extended ($R \sim 2000$ AU) and massive ($M \gtrsim 10^6 M_\odot$) systems. These results suggest LRDs as a distinct class of AGN with stellar-like envelopes.

JWST observations have unveiled a population of compact, high-redshift objects with unique V-shaped spectral energy distribution (SED), commonly referred to as “little red dots” (LRDs). Their compactness and broad Balmer emission lines point to the presence of accreting supermassive black holes (SMBHs) (1–4). However, LRDs also exhibit several properties that distinguish

them from typical AGNs: they are unusually faint in the X-ray (5, 6), radio (7), and far-infrared bands (8, 9), often show strong Balmer absorption and pronounced Balmer breaks (10–14). These puzzling characteristics challenge our current understanding of AGN physics and galaxy-black hole coevolution, suggesting that LRDs may represent a transitional or previously unexplored phase of black hole growth in the early universe (15).

The variability of LRDs offers a powerful probe into their underlying physical nature. Measuring potential time lags between variations in the UV/optical continuum and broad-line emission can reveal the relative geometry of the SMBH, the broad-line region, and the dense gas envelope responsible for strong Balmer breaks and absorption features (14, 16–19). Surprisingly, most LRDs display little to no photometric variability ($\lesssim 5\%$) over an observed timescale of ~ 3 years (20–23). Strong gravitational lensing of LRDs by massive clusters provides a unique opportunity to probe variability over decades, leveraging time delays (Δt_{grav}) that can span tens of years between multiple images. To date, only two multiply imaged LRDs, A2744-QSO1 ($z = 7.04$, $\Delta t_{\text{grav}} \sim 20$ years) (24, 25) in Abell 2744 and A383-LRD1 ($z = 6.02$, $\Delta t_{\text{grav}} \sim 5$ years) in Abell 383 (26), has been reported. A2744-QSO1 hints at changes in emission-line equivalent width (EWs; but not in continuum luminosity or color) over a rest-frame time delay of ~ 2.7 years (17, 25). These timescales remain far shorter than the expected envelope dynamical timescale (t_{dyn} , see Equation 1 below) of several tens of years, which would be the characteristic variability timescale of LRD envelopes (18, 27, 28). More multiply imaged LRDs with longer time delays are needed to explore longer-term variability and establish its universality.

Discovery of two multiply imaged LRDs

The two lensed LRDs in RXC J2211–0350 were first identified through our systematic search for strongly lensed LRDs using archival JWST/NIRCam imaging of over 140 galaxy clusters, primarily from the Strong LensIng and Cluster Evolution (SLICE; PID: 5594) program (29). Subsequent deep 10-band NIRCam imaging from the Vast Exploration for Nascent, Unexplored Sources (VENUS; PID: 6882) program, taken on October 16, 2025, reveals their characteristic V-shape continuum and compact morphology (Figure S1 and S2), establishing both as bona fide LRD candidates awaiting spectroscopic confirmation. Our cluster mass model confirms the multiple images from

both systems, which are gravitationally lensed into four and five distinct images, respectively, by the massive cluster potential of RXC J2211–0350 at $z = 0.397$. One of them forms a perfect Einstein cross in the sky as shown in Figure 1. They are thus dubbed R2211-RX1 and R2211-RX2 (RX for “red cross”). The source-plane positions (Figure S4) demonstrate that both sources reside in a potential galaxy overdensity encompassing nine objects at similar photometric redshift (z_{phot}) and enclosed in a circle with radius of $\sim 10''$ (corresponding to ~ 70 kpc at $z \sim 4.3$). We adopt the most probable redshift of $z_{\text{phot}} \sim 4.3$ of this structure as the fiducial redshift of the two LRDs (see Materials and Methods). This value aligns with their z_{phot} derived from the empirical LRD templates (Figure S1 and S5) and the geometric redshift from the cluster mass model. To date, RXC J2211–0350 hosts the largest known number of multiply imaged LRDs in any galaxy cluster observed by JWST.

Gravitational lensing not only magnifies these intrinsically faint sources but also introduces time delays of decades to over a century among their multiple images. We update the strong cluster mass model of RXC J2211–0350 constructed with *glafic* (30, 31), taking advantage of the newly obtained JWST imaging data (Materials and Methods). The cluster mass model is tightly constrained with 146 multiple images from 43 sources, as shown in Figure S3 and Table S2. For R2211-RX1 and R2211-RX2, the magnifications and time delays derived by the cluster mass model are listed in Table 1. The magnifications for most images range from 2-4, reaching ~ 8.7 for R2211-RX2.5, with typical uncertainties of order ~ 0.1 - 0.2 . The blackbody fitting to the intrinsic SEDs below yields bolometric luminosities for R2211-RX1 and R2211-RX2 of $2.38^{+0.04}_{-0.05} \times 10^{44} \text{ erg s}^{-1}$ and $2.54^{+0.32}_{-0.33} \times 10^{43} \text{ erg s}^{-1}$, respectively. These values are slightly higher than those estimated from L_{5100} (inferred using the intrinsic F300M photometry) using the L_{5100} -based bolometric correction in (32). Assuming the Eddington ratio to be unity, the corresponding black hole masses (M_{BH}) are estimated to be $1.9 \times 10^6 M_{\odot}$ and $2 \times 10^5 M_{\odot}$. Thanks to a large cluster mass ($M \approx 8.1 \times 10^{14} M_{\odot}$ within 500 kpc) and a large Einstein radius ($\Theta_{\text{E}} \approx 47.5''$ at $z \approx 4.3$), the lens model predicts that the relative time delays (observed-frame) between the multiple images span a uniquely long and broad range: ~ 80 - 130 yr for R2211-RX1, and ~ 20 - 160 yr for R2211-RX2, substantially exceeding that of other multiply imaged LRDs (17, 24–26).

LRD variability observed on a century-scale

We use magnification-corrected photometry to investigate their variability (Materials and Methods). We account for both photometric and magnification uncertainties in the error bars. In the short-wavelength (SW) bands, the signal-to-noise ratios (S/Ns) are low because the LRDs are faint in the rest-frame UV. To improve sensitivity, we stack the SW bands (F090W, F115W, and F150W) using a bandpass-weighted flux average for each image. Figures 2(A) and Figure S6 show the delensed photometric light curves of R2211-RX1 and R2211-RX2 in the JWST filters, respectively. To quantify the degree of variability, we define the reduced chi-square χ_v^2 relative to a constant mean flux, as indicated in the Figures.

For R2211-RX1, no significant variability is observed in most bands blueward F200W (i.e., rest-frame $< 3800 \text{ \AA}$) with $\chi_v^2 < 1$, even after stacking. The exception is F150W2, which covers slightly longer wavelengths than F200W. In contrast, the long-wavelength (LW) bands show consistent and coordinated variability across different bands, with amplitudes up to $|\Delta m| \sim 0.7 \text{ mag}$, $S/N \sim 4$, and $\chi_v^2 = 18.4$. Assuming no intrinsic variability, the resulting χ_v^2 values for bands redder than F210M are all significantly greater than unity. Such behavior resembles the visible but $< 3\sigma$ continuum trend seen in the light curves of A2744-QSO1 (25), which was interpreted as no continuum variability due to its low statistical significance. Compared to that case, R2211-RX1 provides a ~ 10 times longer rest-frame time baseline and exhibits a larger variability amplitude. For R2211-RX2, no significant variability is detected in most bands, with the amplitude constrained to $\Delta m \lesssim 0.3 \text{ mag}$. In several bands, we find tentative hints of variability, with $\Delta m_{\text{max}} \sim 0.5\text{--}0.9 \text{ mag}$ at $\sim 2.7\sigma$ and $\chi_v^2 \gtrsim 2$. We caution the faintness of R2211-RX2 in the rest-frame UV (28 \sim 29 mag with lensing magnification) and strong intracluster light background for R2211-RX2.1/2. Further monitoring with deeper JWST imaging is required to confirm this variability. We also examine the short-term variability of R2211-RX1 and R2211-RX2 by comparing the SLICE F322W2 photometry with the VENUS synthetic F277W+F356W measurements over a ~ 1 -year baseline (see Figure S7), and find no significant variability.

Systematic uncertainties in the lensing magnification are the primary source of error for our variability analysis. We perform tests on 12 other multiply imaged systems with $z_{\text{phot}} > 3$ in the same field and find no significant flux and color variations (Figure 2c), confirming the reliability

of our cluster mass model. Microlensing and “millilensing” effects by cluster stars and dark matter subhalos are expected to be negligible (Supplementary Text). The lack of variability in R2211-RX1’s SW bands and R2211-RX2’s bands further supports that their magnification correction is self-consistent. We also detected significant bluer-when-brighter rest-frame optical color variations of R2211-RX1 (Figure 2b), which confirms that the observed variability is intrinsic, since lensing can introduce flux anomalies but not color ones. Other possible systematics, such as spatial PSF variation, depth differences, or contamination (22, 23, 25), cannot reproduce the coherent, multi-band behavior we observe. These tests collectively demonstrate that the detected variability arises from the source itself rather than from lensing or instrumental effects.

Signatures of opacity-driven pulsation

The detection of significant optical variability in R2211-RX1 provides the first robust evidence that some LRDs undergo continuum luminosity changes, underscoring their unique nature. Unlike normal AGNs, which commonly show detectable variability at month-year timescales (33), R2211-RX1 (as well as other LRDs) shows no significant short-term variability between the SLICE and VENUS epochs (rest-frame ~ 0.2 yr; see Figure S7), but varies on much longer timescales (rest-frame > 20 years). Such behavior is expected if LRDs are surrounded by a dense, optically thick envelope resembling a stellar atmosphere (12, 14, 16, 34), as proposed to explain their strong Balmer breaks and absorption features (3, 10, 12, 14). In this framework, any central rapid accretion fluctuations would be damped by the envelope, while the observed variability in R2211-RX1 reflects slow changes in the thermal emission (i.e., blackbody) from such an envelope with photospheric radius $R_{\text{ph}} \sim 1000$ AU and effective temperature $T_{\text{eff}} \sim 5000$ K (18, 19, 28, 35, 36). The observed rest-frame variability timescale closely matches the dynamical time of the gas envelope (28)

$$t_{\text{dyn}} \equiv 2\pi \sqrt{\frac{R_{\text{ph}}^3}{GM_{\text{BH}}}} \approx 44.6 \text{ yr } \lambda_{\text{Edd}}^{3/4} \left(\frac{M_{\text{BH}}}{10^{6.28} M_{\odot}} \right)^{1/4} \left(\frac{T_{\text{eff}}}{5000 \text{ K}} \right)^{-3}, \quad (1)$$

where λ_{Edd} is the Eddington ratio.

We thus model the multi-epoch SEDs of R2211-RX1 with a single-temperature blackbody (18, 19, 35, 37)(Materials and Methods), whose total luminosity $L_{\text{BB}} \propto R_{\text{ph}}^2 T_{\text{eff}}^4$. An epoch-independent power-law component is added to account for the potential host galaxy dominance in rest-frame

UV (14, 17, 28). This simple model provides a reasonable fit to the SEDs of R2211-RX1 (Figure 3A), with $T_{\text{eff}} \sim 4000$ K, $R_{\text{ph}} \sim 2000$ AU, and $L_{\text{BB}} \sim 2 \times 10^{44} \text{ erg s}^{-1}$. The best-fit temperatures increase systematically in the brighter epochs, and the inferred blackbody luminosities roughly follow $L_{\text{BB}} \propto T_{\text{eff}}^4$ (the best-fit relation is $L_{\text{BB}} \propto T_{\text{eff}}^{4.9 \pm 1.0}$) as shown in Figure 3(B). The deviation from $L \propto T_{\text{eff}}^4$ indicates a modest change in the effective emitting radius of ~ 200 AU (10% of the R_{ph}) over ~ 10 years in the rest frame.

Such $L_{\text{BB}} \sim T_{\text{eff}}^4$ behavior is reminiscent of the classical opacity-driven pulsations (κ -mechanism) seen in variable super-giant stars such as Cepheids (38, 39). In those stars, compression of a partially ionized layer (usually He^+ layer) increases its opacity so that radiation is temporarily trapped and energy is stored. The compression also builds up a pressure gradient, driving the layer to expand further than the original oscillation. During expansion, the gas cools and becomes more transparent, the pressure drops, and the layer contracts, completing the cycle. In effect, the layer acts like a heat engine, converting trapped radiation into mechanical work and sustaining the pulsation cycle (40). Similar opacity-driven pulsations have also been predicted for the radiation-dominated envelopes of supermassive stars (SMSs; $\sim 10^3$ - $10^5 M_{\odot}$), which might be the progenitor of high-redshift SMBHs (41–43) and have even been proposed as a possible explanation for LRDs (35, 44). Although the central black hole in an LRD is estimated to be far more massive than typical SMSs, the overall configuration is analogous: both systems are in hydrostatic equilibrium state supported by radiation pressure, and both possess similar surface temperatures and gravity. Within the envelope, regions with temperatures of order $\sim 3 \times 10^4$ K would naturally create a He^+ partial ionization zone that acts as an engine region. Therefore, a similar physical mechanism could give rise to the slow, periodic rest-frame optical variability observed for R2211-RX1, while its rest-frame UV emission, dominated by the host galaxy, remains stable.

Previous studies show that SMSs are unstable primarily to radial perturbations (42, 45). Motivated by this, we examine whether the current limited multi-epoch data of R2211-RX1 are compatible with a minimal description of pulsation based on a single fundamental radial mode (f-mode). In a polytropic envelope, the fundamental eigenfrequency solved by (46) naturally gives a pulsation period that can be expressed as $T_0 = f_0 t_{\text{dyn}}$, where $f_0 = 0.37$ is set by the numerical fundamental eigenvalue from (46). Substituting the inferred properties of R2211-RX1 (i.e.,

$T_{\text{eff}} = 4000 \text{ K}$ and $M_{\text{BH}} = 10^{6.28} M_{\odot}$) in Equation (1), the resulting pulsation period is $T_0 = 32 \text{ yr}$. We model the variability in all bands redder than F210M using a sinusoid (i.e., f-mode) model with this fixed period (Materials and Methods). The sinusoid phase is tied across all bands, while allowing the amplitude and mean flux to vary independently per band. The fitting results are shown in Figure 3(C). All bands are well described by this simple f-mode model, with a total $\chi^2_{\nu} = 0.09$ for 11 degrees of freedom (dof). The F322W2 band includes eight observational points, augmented by synthetic fluxes from the VENUS F277W and F356W bands, and is also well reproduced by the model. While the low χ^2_{ν} suggests potential overfitting, comparably good fits occur only within a narrow strip in the $M_{\text{BH}}-T_{\text{eff}}$ space that corresponds to a proper pulsation period range (Figure S8). The independently inferred M_{BH} and T_{eff} of R2211-RX1 fall precisely within this optimal region, demonstrating that the fit is physically self-consistent rather than an artifact of flexible modeling. Overall, the good agreement across all bands indicates that the pulsation scenario dominated by the f-mode offers a reasonable description of the current observed light curve. Future modeling with improved sampling will enable stronger constraints on additional pulsation modes and the pulsation period, refining this physical picture.

Projecting the illustrative f-mode light curve model into the $T_{\text{eff}}-L_{\text{BB}}$ space with blackbody model visualizes the system’s potential temporal sequence in the pulsation scenario (Materials and Methods). The resulting trajectory in Figure 3(B) shows a counterclockwise loop, resembling that of classical pulsating stars like Cepheids. In this pattern, the envelope is hotter (and smaller) during the brightening phase than the dimming phase at a given luminosity, a consequence of the hysteresis between temperature and radius variations (38, 47)(see also Figure S9). Such a lag arises from finite thermal inertia: when compressed, the gas heats faster than it can radiate, and when expanding, it cools more slowly, mimicking a heat engine in which heating and cooling are out of phase with mechanical motion. Consistent with this picture, the expansion velocity inferred (132 km s^{-1} from R2211-RX1.3 to R2211-RX1.1) is larger than the contraction velocity (61 km s^{-1} from R2211-RX1.1 to R2211-RX1.2), as expected for opacity-driven pulsations. These velocities are obtained by dividing the change in R_{ph} between the epochs by the corresponding rest-frame time intervals. While we caution that this trajectory is a model-dependent inference, the data’s natural accommodation of such a phase lag lends qualitative support to the stellar-like envelope hypothesis.

The pulsation scenario also provides a natural explanation for the observed diversity in the long-term variability of LRDs. Analogous to stars that are variable only within a specific instability strip on the Hertzsprung–Russell (HR) diagram (38), the opacity-driven instability for LRD envelopes likely also depends on their physical properties like temperature and luminosity (or M_{BH}). R2211-RX1, with a relatively cool effective temperature ($T_{\text{eff}} \sim 4000$ K), exhibits strong variability, whereas the hotter system R2211-RX2 ($T_{\text{eff}} \sim 5000$ K) remains stable in the rest-frame optical. This potential temperature dependence also offers a context for the absence of detectable variability in local LRDs, which have $T_{\text{eff}} \sim 5000$ K (19), over the rest-frame ~ 5 -year ZTF baseline (27). These results collectively suggest that the pulsational instability domain for LRDs may be favored in cooler envelopes (e.g., $T_{\text{eff}} \lesssim 5000$ K).

Future monitoring and predictions

While the κ -mechanism can plausibly account for the variability of R2211-RX1, the observed $L_{\text{BB}} \propto T_{\text{eff}}^{4.9 \pm 1.0}$ relation is somewhat steeper than the $L_{\text{BB}} \sim T_{\text{eff}}^4$ slope expected for a quasi-static pulsating photosphere, hinting that variations in the accretion state, which naturally present in AGNs through disc instabilities or changes in accretion rate (48), may also play a role. Adopting a typical optical depth of $\tau \sim 10$, the photon diffusion time $t_{\text{diff}} \sim \tau R_{\text{ph}}/c = 0.1$ yr, implying that the envelope can respond quasi-isobarically to the central luminosity variations. In this scenario, increases in the central ionizing source luminosity would drive simultaneous rises in T_{eff} and R_{ph} ($PR_{\text{ph}}^3 \propto T_{\text{eff}}$), steepening the T_{eff} - L_{BB} slope.

Future JWST multi-cycle spectrophotometric monitoring will be critical to distinguish and confirm these scenarios. Such a campaign bridges two distinct time domains: while multi-cycle observations are essential to capture evolution on timescales of days to years, the time delays between lensed images simultaneously provides baseline extending to decades or even a century. Spectroscopically, pulsation-driven variability should produce detectable velocity shifts (~ 100 km s^{-1}) in absorption lines ($\text{H}\alpha$, $\text{H}\beta$, He I, etc.), if some of them are produced by the gas envelope. Such shifts arise from envelope expansion/contraction (Figure 4A), analogous to pulsating stars (49, 50). Conversely, variability driven by changes in the accretion state may cause the broad lines to vary following the bolometric luminosity change if they are powered by the central BH

(Figure 4B), while narrow forbidden lines originating from the host galaxy remain stable. These predictions can be directly tested through future multi-cycle JWST/NIRSpec prism and high-resolution spectroscopy effectively. Complementarily, multi-epoch JWST imaging observations offer an independent falsifiable test as shown in Figure 4: while accretion state changes imply irregular, aperiodic fluctuations, the pulsation model predicts coherent phase shifts across the lensed images detectable variation of ~ 0.1 mag within 5-10 years. If the real period is significantly shorter, the phase evolution across the images would be correspondingly larger.

The discovery of long-term variability in R2211-RX1 reveals that the dense gas envelope surrounding some early SMBHs could behave remarkably like an enormous, radiation-pressure-dominated stellar atmosphere, providing strong support for the envelope scenario of LRDs and offering insights into black-hole seeding. This finding motivates a broader investigation into the parallels between LRDs and stellar physics, particularly whether these objects occupy an instability strip in the HR diagram or adhere to a Period-Luminosity relation analogous to the Leavitt Law for Cepheids. While confirming such fundamental relations requires a larger sample, cluster-lensed systems like R2211-RX1 and R2211-RX2 offer a unique opportunity to extend the baseline to the century scale, opening a new window to study the nature of LRDs and the formation of the first SMBHs.

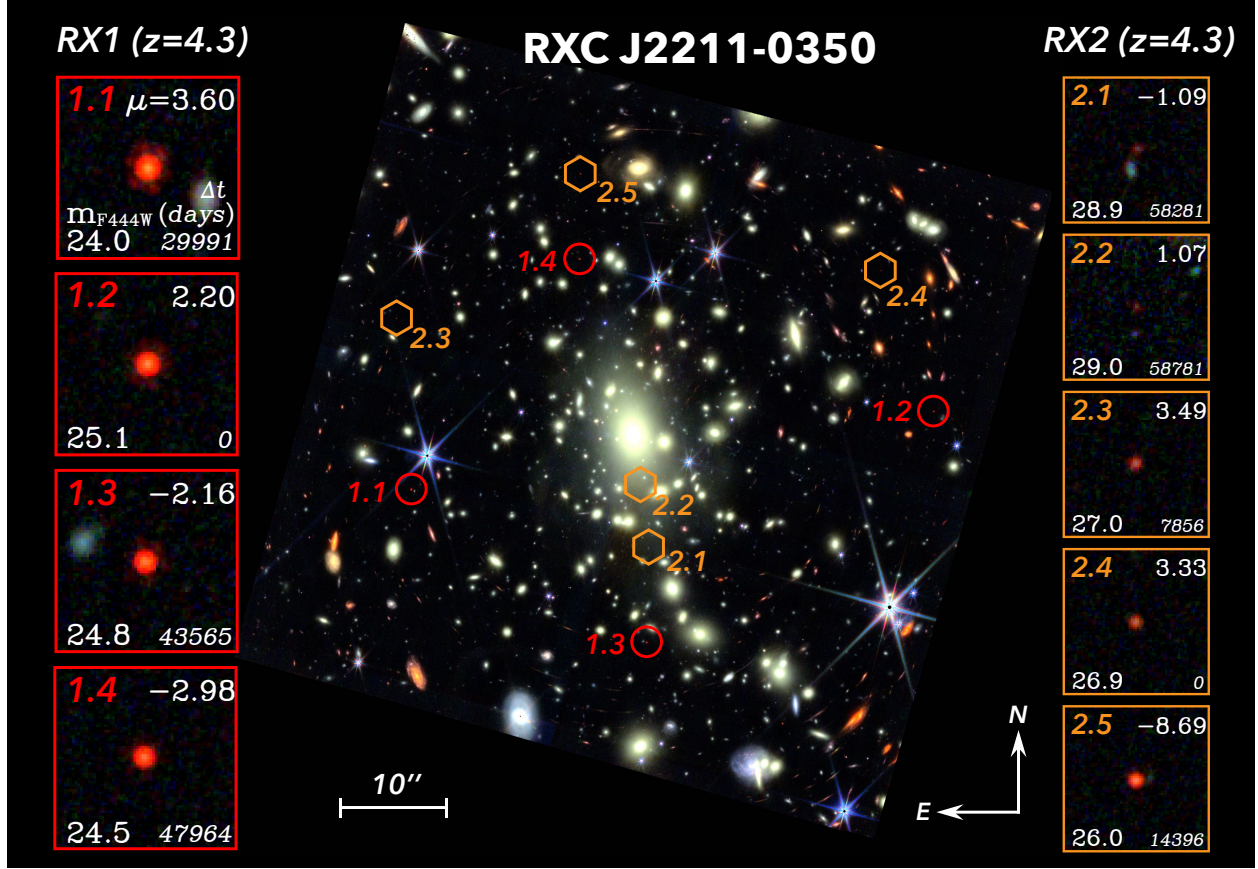


Figure 1: JWST NIRCам color composite image of the galaxy cluster RXC J2211–0350.

Thanks to strong gravitational lensing, two multiply imaged LRDs, dubbed RX1 and RX2, are identified, both with photometric redshifts of $z = 4.3$. The four images of RX1 are marked by red circles (1.1-1.4), and the five images of RX2 are marked by orange hexagons (2.1-2.5). The left (red) and right (orange) panels show zoom-in cutouts for each of these lensed images. In each cutout, the image name is given in the top left, the magnification (μ ; negative value indicates that the image parity is reversed and the image orientation is flipped) calculated from our cluster mass model is in the top right, the measured F444W-band magnitude (not corrected for magnification) is in the bottom left, and the inferred time delay (Δt in days) is in the bottom right. The uncertainties of μ and Δt are typically $\lesssim 5\%$.

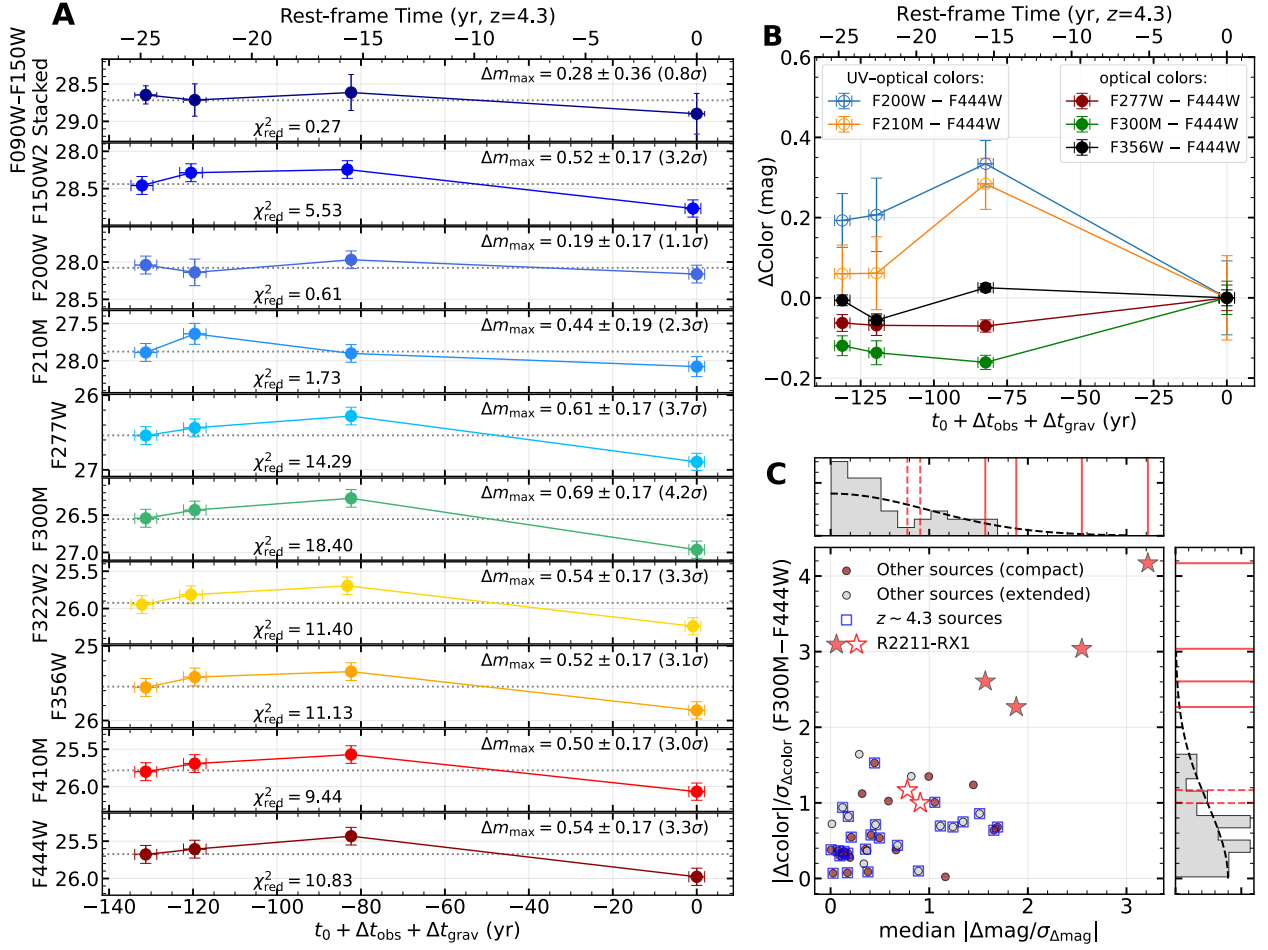


Figure 2: Brightness and color variability of R2211-RX1. (A) De-magnified light curves of R2211-RX1 in each JWST band, incorporating the gravitational lens time delays Δt_{grav} given in Table 1. t_0 is the VENUS observation date. Dotted lines show the mean magnitude of each band, and the error bars include magnification uncertainties. We show the maximal Δm and χ^2_{ν} values assuming no variability for each band. (B) Multi-band color evolution of R2211-RX1, with x-axis the same as (A). The y-axis shows the color difference relative to image R2211-RX1.2. (C) S/N distribution of brightness and color (F300M–F444W) variability between all epochs pairs for R2211-RX1 and the other 12 multiply imaged sources with $z_{\text{phot}} > 3$. Sources with $z_{\text{phot}} \sim 4.3$ in Figure S4 are marked with blue squares. For each epoch pair, the brightness variability S/N is measured as the median S/N of Δmag across the F200W and redder bands to reflect the overall variability of the SED. In the top/right panels, red lines indicate R2211-RX1, and the gray histogram represents the other sources. The two R2211-RX1 pairs with the shortest observed-frame intervals (10 and 36 yr) have $S/N \sim 1$ and are shown as open stars, while all others have $S/N > 2$. The S/N of the other sources are broadly consistent with a one-sided normal distribution and mostly below 1, suggesting that the measured variability of R2211-RX1 is not biased by systematic errors in magnification.

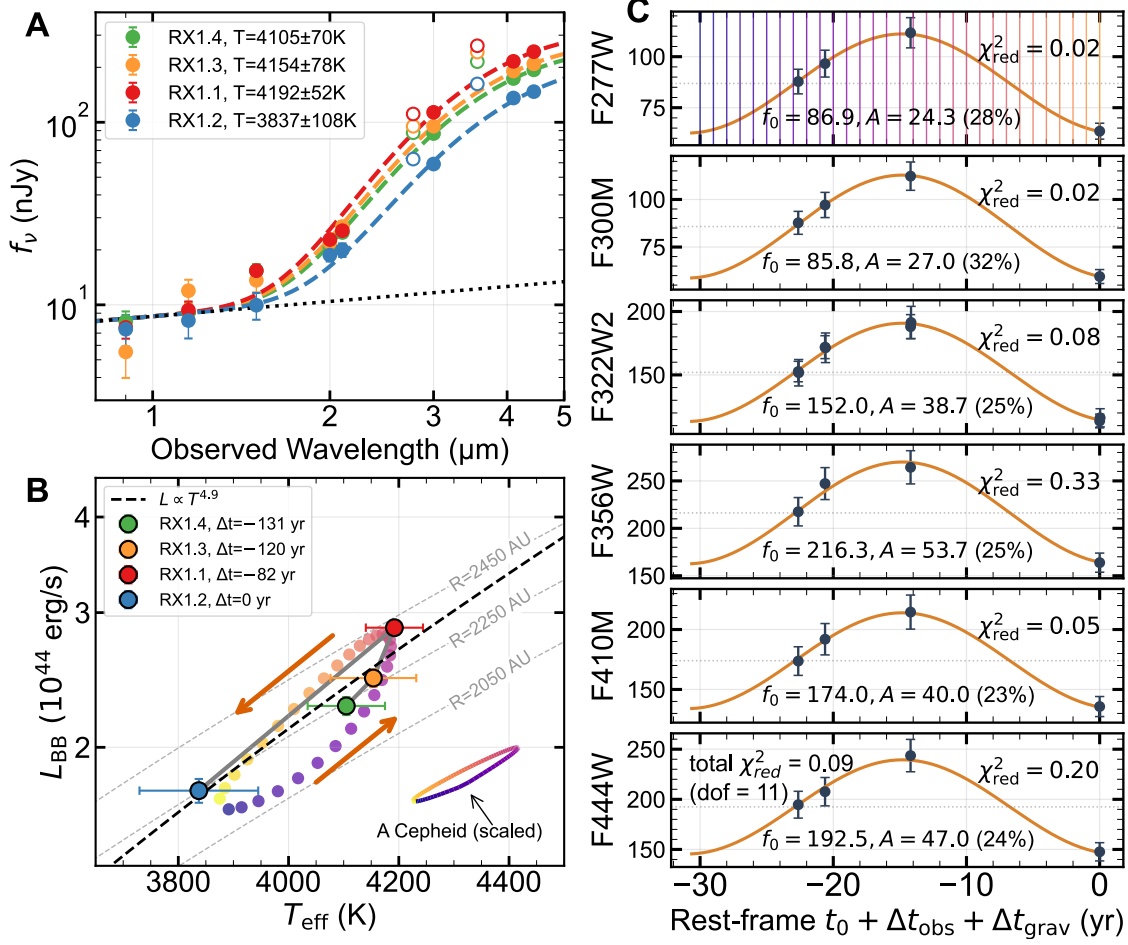


Figure 3: SED modeling, light curve modeling, and $T_{\text{eff}}\text{-}L_{\text{BB}}$ evolution of R2211-RX1. (A) Intrinsic SEDs and best-fit models for the four multiple images of R2211-RX1. Filled/open circles mark fitted/excluded (potentially affected by strong emission lines) bands. The dashed colored lines show the best-fit single-temperature blackbody + shared power law (black dotted line). (B) T_{eff} versus L_{BB} for the four images of R2211-RX1. The solid gray line connects the four images, ordered by their relative time delays. The dashed black line indicates the best-fit power-law scaling $L_{\text{BB}} \propto T_{\text{eff}}^{4.9 \pm 1.0}$. Colored dots denote the evolutionary sequence derived from the light curve fitting in (C), showing a counterclockwise progression in chronological order. We also show the $T_{\text{eff}}\text{-}L_{\text{BB}}$ circle of a Cepheid with mean T_{eff} and L_{BB} scaled and color matched to the phase of the LRD circle in the bottom right. Dashed gray curves denote loci of constant blackbody radius. (C) Light curve (delensed flux in nJy) fitting results of R2211-RX1. Observed light curves (gray points) and best-fit models (orange curves) are shown, with best-fit amplitude, phase, and χ^2_ν marked in each band. The total χ^2_ν is indicated in the upper left of the F444W band panel. Vertical lines in the top panel mark the 40 epochs sampled at one-year intervals, with colors corresponding to those in (B).

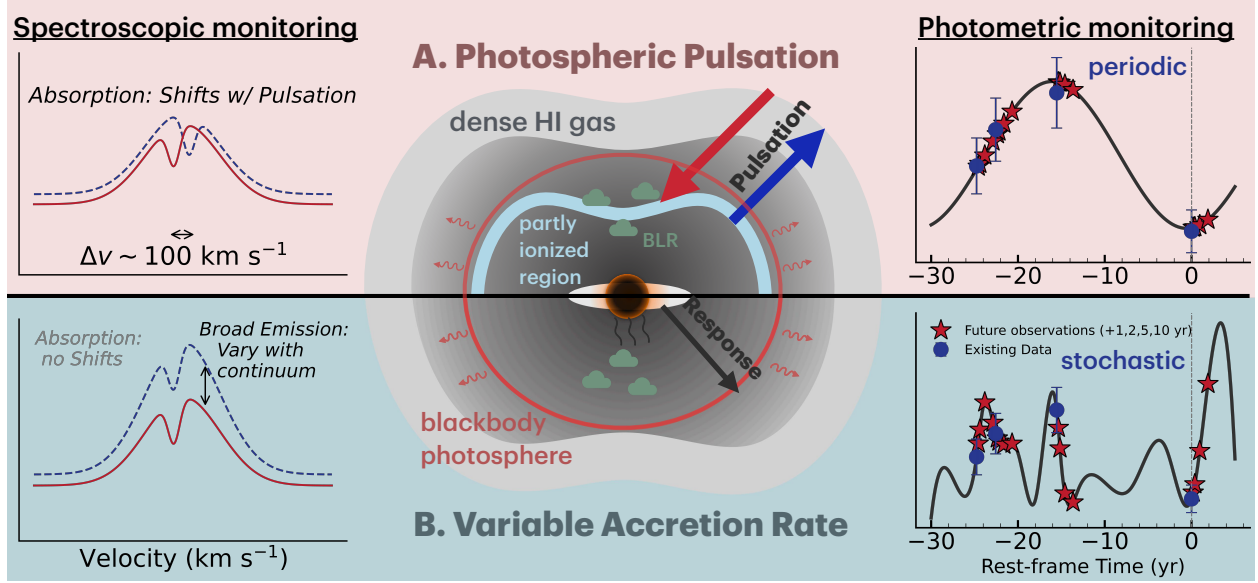


Figure 4: Conceptual models of LRD dense gas envelopes under two scenarios. (A) Under the photospheric pulsation interpretation, we expect the dense H I gas to undergo similar pulsation as the partly ionized region, producing velocity shift of certain absorption lines among multiple images and periodicity in the light curve that can be obtained through long-term spectrophotometric monitoring. **(B)** Under the variable accretion state interpretation, we expect the variation of broad emission line strength correlated with the underlying continuum while no obvious velocity shift in absorption lines, and the resultant long-term light curve will appear stochastic. Expected outcomes from future spectroscopic (left) and photometric (right) monitoring are indicated.

Table 1: Coordinates, lensing magnifications, and gravitational lens time delays of the multiple images of R2211-RX1 and R2211-RX2. Negative lensing magnifications indicate that the image parity is reversed (i.e., the image orientation is flipped).

ID	R.A.	Decl.	μ	μ_{tan}	μ_{rad}	$-\Delta t_{\text{grav}}$ (days)
R2211-RX1.1	332.95385	-3.83207	$3.60^{+0.14}_{-0.14}$	$3.25^{+0.12}_{-0.08}$	$1.10^{+0.03}_{-0.01}$	29990^{+680}_{-660}
R2211-RX1.2	332.92441	-3.82768	$2.20^{+0.07}_{-0.07}$	$2.15^{+0.05}_{-0.04}$	$1.01^{+0.02}_{-0.01}$	0
R2211-RX1.3	332.94059	-3.84067	$-2.16^{+0.07}_{-0.09}$	$-1.70^{+0.05}_{-0.04}$	$1.31^{+0.01}_{-0.06}$	43570^{+970}_{-910}
R2211-RX1.4	332.94437	-3.81911	$-2.98^{+0.12}_{-0.15}$	$-1.88^{+0.07}_{-0.06}$	$1.63^{+0.01}_{-0.07}$	47960^{+970}_{-990}
R2211-RX2.1	332.94046	-3.83532	$-1.09^{+0.05}_{-0.05}$	$-0.64^{+0.02}_{-0.01}$	$1.71^{+0.05}_{-0.03}$	58300^{+1100}_{-1100}
R2211-RX2.2	332.94092	-3.83182	$1.07^{+0.08}_{-0.10}$	$-0.38^{+0.02}_{-0.00}$	$-2.83^{+0.17}_{-0.15}$	58800^{+1100}_{-1100}
R2211-RX2.3	332.95469	-3.82245	$3.49^{+0.14}_{-0.14}$	$3.20^{+0.09}_{-0.10}$	$1.09^{+0.01}_{-0.02}$	7860^{+460}_{-380}
R2211-RX2.4	332.92738	-3.81977	$3.33^{+0.13}_{-0.11}$	$3.29^{+0.06}_{-0.08}$	$1.01^{+0.02}_{-0.02}$	0
R2211-RX2.5	332.94432	-3.81431	$-8.69^{+0.76}_{-0.84}$	$-6.63^{+0.65}_{-0.52}$	$1.32^{+0.03}_{-0.02}$	14400^{+660}_{-600}

References and Notes

1. Y. Harikane, *et al.*, A JWST/NIRSpec First Census of Broad-line AGNs at $z = 4-7$: Detection of 10 Faint AGNs with $M_{BH} 10^6-10^8 M_{\odot}$ and Their Host Galaxy Properties. *Astrophys. J.* **959** (1), 39 (2023), doi:10.3847/1538-4357/ad029e.
2. J. E. Greene, *et al.*, UNCOVER Spectroscopy Confirms the Surprising Ubiquity of Active Galactic Nuclei in Red Sources at $z > 5$. *Astrophys. J.* **964** (1), 39 (2024), doi:10.3847/1538-4357/ad1e5f.
3. J. Matthee, *et al.*, Little Red Dots: An Abundant Population of Faint Active Galactic Nuclei at $z \sim 5$ Revealed by the EIGER and FRESCO JWST Surveys. *Astrophys. J.* **963** (2), 129 (2024), doi:10.3847/1538-4357/ad2345.
4. D. D. Kocevski, *et al.*, The Rise of Faint, Red Active Galactic Nuclei at $z > 4$: A Sample of Little Red Dots in the JWST Extragalactic Legacy Fields. *Astrophys. J.* **986** (2), 126 (2025), doi:10.3847/1538-4357/adbc7d.
5. M. Yue, *et al.*, Stacking X-Ray Observations of “Little Red Dots”: Implications for Their Active Galactic Nucleus Properties. *Astrophys. J. Lett.* **974** (2), L26 (2024), doi:10.3847/2041-8213/ad7eba.
6. R. Maiolino, *et al.*, JWST meets Chandra: a large population of Compton thick, feedback-free, and intrinsically X-ray weak AGN, with a sprinkle of SNe. *Mon. Not. R. Astron. Soc.* **538** (3), 1921–1943 (2025), doi:10.1093/mnras/staf359.
7. G. Mazzolari, *et al.*, The radio properties of the JWST-discovered AGN. *arXiv e-prints* arXiv:2412.04224 (2024), doi:10.48550/arXiv.2412.04224.
8. P. G. Pérez-González, *et al.*, What Is the Nature of Little Red Dots and what Is Not, MIRI SMILES Edition. *Astrophys. J.* **968** (1), 4 (2024), doi:10.3847/1538-4357/ad38bb.
9. C. C. Williams, *et al.*, The Galaxies Missed by Hubble and ALMA: The Contribution of Extremely Red Galaxies to the Cosmic Census at $3 < z < 8$. *Astrophys. J.* **968** (1), 34 (2024), doi:10.3847/1538-4357/ad3f17.

10. X. Lin, *et al.*, A SPectroscopic survey of biased halos In the Reionization Era (ASPIRE): Broad-line AGN at $z = 4 - 5$ revealed by JWST/NIRCam WFSS. *arXiv e-prints* arXiv:2407.17570 (2024), doi:10.48550/arXiv.2407.17570.
11. B. Wang, *et al.*, RUBIES: Evolved Stellar Populations with Extended Formation Histories at $z \sim 7-8$ in Candidate Massive Galaxies Identified with JWST/NIRSpec. *Astrophys. J. Lett.* **969** (1), L13 (2024), doi:10.3847/2041-8213/ad55f7.
12. A. de Graaff, *et al.*, A remarkable ruby: Absorption in dense gas, rather than evolved stars, drives the extreme Balmer break of a little red dot at $z = 3.5$. *Astron. Astrophys.* **701**, A168 (2025), doi:10.1051/0004-6361/202554681.
13. I. Juodžbalis, *et al.*, JADES: comprehensive census of broad-line AGN from Reionization to Cosmic Noon revealed by JWST. *arXiv e-prints* arXiv:2504.03551 (2025).
14. R. P. Naidu, *et al.*, A “Black Hole Star” Reveals the Remarkable Gas-Enshrouded Hearts of the Little Red Dots. *arXiv e-prints* arXiv:2503.16596 (2025), doi:10.48550/arXiv.2503.16596.
15. K. Inayoshi, Little Red Dots as the Very First Activity of Black Hole Growth. *Astrophys. J. Lett.* **988** (1), L22 (2025), doi:10.3847/2041-8213/adea66.
16. K. Inayoshi, R. Maiolino, Extremely Dense Gas around Little Red Dots and High-redshift Active Galactic Nuclei: A Nonstellar Origin of the Balmer Break and Absorption Features. *Astrophys. J. Lett.* **980** (2), L27 (2025), doi:10.3847/2041-8213/adaebd.
17. X. Ji, *et al.*, BlackTHUNDER – A non-stellar Balmer break in a black hole-dominated little red dot at $z = 7.04$. *arXiv e-prints* arXiv:2501.13082 (2025), doi:10.48550/arXiv.2501.13082.
18. D. Kido, K. Ioka, K. Hotokezaka, K. Inayoshi, C. M. Irwin, Black Hole Envelopes in Little Red Dots. *arXiv e-prints* arXiv:2505.06965 (2025), doi:10.48550/arXiv.2505.06965.
19. X. Lin, *et al.*, The Discovery of Little Red Dots in the Local Universe: Signatures of Cool Gas Envelopes. *arXiv e-prints* arXiv:2507.10659 (2025), doi:10.48550/arXiv.2507.10659.

20. M. Kokubo, Y. Harikane, Challenging the AGN scenario for JWST/NIRSpec broad H α emitters/Little Red Dots in light of non-detection of NIRCам photometric variability and X-ray. *arXiv e-prints* arXiv:2407.04777 (2024), doi:10.48550/arXiv.2407.04777.
21. W. L. Tee, X. Fan, F. Wang, J. Yang, Lack of Rest-frame Ultraviolet Variability in Little Red Dots Based on HST and JWST Observations. *Astrophys. J. Lett.* **983** (1), L26 (2025), doi:10.3847/2041-8213/adc5e3.
22. Z. Stone, *et al.*, NEXUS: A Search for Nuclear Variability with the First Two JWST NIRCам Epochs. *arXiv e-prints* arXiv:2509.19585 (2025), doi:10.48550/arXiv.2509.19585.
23. Z. Zhang, L. Jiang, W. Liu, L. C. Ho, Analysis of Multi-epoch JWST Images of ~ 300 Little Red Dots: Tentative Detection of Variability in a Minority of Sources. *Astrophys. J.* **985** (1), 119 (2025), doi:10.3847/1538-4357/adcb3e.
24. L. J. Furtak, *et al.*, JWST UNCOVER: Extremely Red and Compact Object at $z_{phot} \simeq 7.6$ Triply Imaged by A2744. *Astrophys. J.* **952** (2), 142 (2023), doi:10.3847/1538-4357/acdc9d.
25. L. J. Furtak, *et al.*, Investigating photometric and spectroscopic variability in the multiply imaged little red dot A2744-QSO1. *Astron. Astrophys.* **698**, A227 (2025), doi:10.1051/0004-6361/202554110.
26. M. Golubchik, *et al.*, VENUS: When Red meets Blue – A multiply imaged Little Red Dot with an apparent blue companion behind the galaxy cluster Abell 383. *arXiv e-prints* arXiv:2512.02117 (2025).
27. C. J. Burke, Z. Stone, Y. Shen, Y.-F. Jiang, Too Quiet for Comfort: Local Little Red Dots Lack Variability over Decades. *arXiv e-prints* arXiv:2511.16082 (2025), doi:10.48550/arXiv.2511.16082.
28. K. Inayoshi, K. Murase, K. Kashiyama, Spectral Uniformity of Little Red Dots: A Natural Outcome of Coevolving Seed Black Holes and Nascent Starbursts. *arXiv e-prints* arXiv:2509.19422 (2025), doi:10.48550/arXiv.2509.19422.

29. C. Cerny, *et al.*, Strong LensIng and Cluster Evolution (SLICE) with JWST: Early Results, Lens Models, and High-Redshift Detections. *arXiv e-prints* arXiv:2503.17498 (2025), doi: 10.48550/arXiv.2503.17498.
30. M. Oguri, The Mass Distribution of SDSS J1004+4112 Revisited. *Publ. Astron. Soc. Jpn* **62**, 1017 (2010), doi:10.1093/pasj/62.4.1017.
31. M. Oguri, Fast Calculation of Gravitational Lensing Properties of Elliptical Navarro-Frenk-White and Hernquist Density Profiles. *Publ. Astron. Soc. Pacific* **133** (1025), 074504 (2021), doi:10.1088/1538-3873/ac12db.
32. J. E. Greene, *et al.*, What you see is what you get: empirically measured bolometric luminosities of Little Red Dots. *arXiv e-prints* arXiv:2509.05434 (2025), doi:10.48550/arXiv.2509.05434.
33. C. L. MacLeod, *et al.*, Modeling the Time Variability of SDSS Stripe 82 Quasars as a Damped Random Walk. *Astrophys. J.* **721** (2), 1014–1033 (2010), doi:10.1088/0004-637X/721/2/1014.
34. V. Rusakov, *et al.*, JWST’s little red dots: an emerging population of young, low-mass AGN cocooned in dense ionized gas. *arXiv e-prints* arXiv:2503.16595 (2025), doi:10.48550/arXiv.2503.16595.
35. M. C. Begelman, J. Dexter, Little Red Dots As Late-stage Quasi-stars. *arXiv e-prints* arXiv:2507.09085 (2025), doi:10.48550/arXiv.2507.09085.
36. H. Liu, Y.-F. Jiang, E. Quataert, J. E. Greene, Y. Ma, The Balmer Break and Optical Continuum of Little Red Dots From Super-Eddington Accretion. *arXiv e-prints* arXiv:2507.07190 (2025), doi:10.48550/arXiv.2507.07190.
37. A. Torralba, *et al.*, The warm outer layer of a Little Red Dot as the source of [Fe II] and collisional Balmer lines with scattering wings. *arXiv e-prints* arXiv:2510.00103 (2025), doi: 10.48550/arXiv.2510.00103.
38. J. P. Cox, *Theory of Stellar Pulsation. (PSA-2), Volume 2*, vol. 2 (1980).
39. Y. Li, Z. G. Gong, Red supergiant variables in the Large Magellanic Cloud : their evolution and pulsations. *Astron. Astrophys.* **289**, 449–457 (1994).

40. A. S. Eddington, The pulsation theory of Cepheid variables. *The Observatory* **40**, 290–293 (1917).
41. Y. Osaki, The Pulsation and Evolution of Super-Massive Stars. *Publ. Astron. Soc. Jpn* **18** (4), 384–420 (1966), doi:10.1093/pasj/18.4.384.
42. I. Baraffe, A. Heger, S. E. Woosley, On the Stability of Very Massive Primordial Stars. *Astrophys. J.* **550** (2), 890–896 (2001), doi:10.1086/319808.
43. K. Inayoshi, T. Hosokawa, K. Omukai, Pulsational instability of supergiant protostars: do they grow supermassive by accretion? *Mon. Not. R. Astron. Soc.* **431** (4), 3036–3044 (2013), doi:10.1093/mnras/stt362.
44. D. Nandal, A. Loeb, Supermassive Stars Match the Spectral Signatures of JWST’s Little Red Dots. *arXiv e-prints* arXiv:2507.12618 (2025), doi:10.48550/arXiv.2507.12618.
45. T. Sonoi, H. Umeda, Vibrational instability of Population III very massive main-sequence stars due to the ϵ -mechanism. *Mon. Not. R. Astron. Soc.* **421** (1), L34–L38 (2012), doi:10.1111/j.1745-3933.2011.01201.x.
46. M. Schwarzschild, Overtone Pulsations for the Standard Model. *Astrophys. J.* **94**, 245 (1941), doi:10.1086/144329.
47. G. Bono, M. Marconi, R. F. Stellingwerf, Classical Cepheid pulsation models — VI. The Hertzsprung progression. *Astron. Astrophys.* **360**, 245–262 (2000), doi:10.48550/arXiv.astro-ph/0006229.
48. C. Ricci, B. Trakhtenbrot, Changing-look active galactic nuclei. *Nature Astronomy* **7**, 1282–1294 (2023), doi:10.1038/s41550-023-02108-4.
49. O. K. L. Petterson, P. L. Cottrell, M. D. Albrow, A. Fokin, A spectroscopic study of bright southern Cepheids - a high-resolution view of Cepheid atmospheres. *Mon. Not. R. Astron. Soc.* **362** (4), 1167–1182 (2005), doi:10.1111/j.1365-2966.2005.09332.x.
50. V. Houdé, *et al.*, Pulsating chromosphere of classical Cepheids. Calcium infrared triplet and H α profile variations. *Astron. Astrophys.* **641**, A74 (2020), doi:10.1051/0004-6361/202037795.

51. M. B. Bagley, *et al.*, CEERS Epoch 1 NIRCam Imaging: Reduction Methods and Simulations Enabling Early JWST Science Results. *Astrophys. J. Lett.* **946** (1), L12 (2023), doi:10.3847/2041-8213/acbb08.
52. D. Burgarella, V. Buat, J. Iglesias-Páramo, Star formation and dust attenuation properties in galaxies from a statistical ultraviolet-to-far-infrared analysis. *Mon. Not. R. Astron. Soc.* **360** (4), 1413–1425 (2005), doi:10.1111/j.1365-2966.2005.09131.x.
53. M. Boquien, *et al.*, CIGALE: a python Code Investigating GALaxy Emission. *Astron. Astrophys.* **622**, A103 (2019), doi:10.1051/0004-6361/201834156.
54. B. Häußler, *et al.*, MegaMorph - multiwavelength measurement of galaxy structure: complete Sérsic profile information from modern surveys. *Mon. Not. R. Astron. Soc.* **430** (1), 330–369 (2013), doi:10.1093/mnras/sts633.
55. M. Vika, *et al.*, MegaMorph - multiwavelength measurement of galaxy structure. Sérsic profile fits to galaxies near and far. *Mon. Not. R. Astron. Soc.* **435** (1), 623–649 (2013), doi:10.1093/mnras/stt1320.
56. E. Bertin, S. Arnouts, SExtractor: Software for source extraction. *Astron. Astrophys. Suppl.* **117**, 393–404 (1996), doi:10.1051/aas:1996164.
57. D. Coe, *et al.*, RELICS: Reionization Lensing Cluster Survey. *Astrophys. J.* **884** (1), 85 (2019), doi:10.3847/1538-4357/ab412b.
58. H. Bushouse, *et al.*, JWST Calibration Pipeline (2025), doi:10.5281/zenodo.15178003, <https://github.com/spacetelescope/jwst>.
59. A. Dey, *et al.*, Overview of the DESI Legacy Imaging Surveys. *Astron. J.* **157** (5), 168 (2019), doi:10.3847/1538-3881/ab089d.
60. Gaia Collaboration, *et al.*, Gaia Data Release 2. Summary of the contents and survey properties. *Astron. Astrophys.* **616**, A1 (2018), doi:10.1051/0004-6361/201833051.

61. F. Sun, *et al.*, Slitless Areal Pure-Parallel High-Redshift Emission Survey (SAPPHIRES): Early Data Release of Deep JWST/NIRCam Images and Spectra in MACS J0416 Parallel Field. *arXiv e-prints* arXiv:2503.15587 (2025), doi:10.48550/arXiv.2503.15587.
62. L. Bradley, *et al.*, astropy/photutils: 1.12.0 (2024), doi:10.5281/zenodo.10967176, <https://doi.org/10.5281/zenodo.10967176>.
63. C. Cerny, *et al.*, RELICS: Strong Lens Models for Five Galaxy Clusters from the Reionization Lensing Cluster Survey. *Astrophys. J.* **859** (2), 159 (2018), doi:10.3847/1538-4357/aabe7b.
64. J. F. Navarro, C. S. Frenk, S. D. M. White, A Universal Density Profile from Hierarchical Clustering. *Astrophys. J.* **490** (2), 493–508 (1997), doi:10.1086/304888.
65. Y. Liu, M. Oguri, S. Cao, Hubble constant from the cluster-lensed quasar system SDSS J 1004 +4112 : Investigation of the lens model dependence. *Physical Review D* **108** (8), 083532 (2023), doi:10.1103/PhysRevD.108.083532.
66. D. J. Setton, *et al.*, Little Red Dots at an Inflection Point: Ubiquitous “V-Shaped” Turnover Consistently Occurs at the Balmer Limit. *arXiv e-prints* arXiv:2411.03424 (2024), doi:10.48550/arXiv.2411.03424.
67. R. E. Hviding, *et al.*, RUBIES: A Spectroscopic Census of Little Red Dots; All V-Shaped Point Sources Have Broad Lines. *arXiv e-prints* arXiv:2506.05459 (2025), doi:10.48550/arXiv.2506.05459.
68. A. de Graaff, *et al.*, RUBIES: A complete census of the bright and red distant Universe with JWST/NIRSpec. *Astron. Astrophys.* **697**, A189 (2025), doi:10.1051/0004-6361/202452186.
69. R. Bezanson, *et al.*, The JWST UNCOVER Treasury Survey: Ultradeep NIRSpec and NIRCam Observations before the Epoch of Reionization. *Astrophys. J.* **974** (1), 92 (2024), doi:10.3847/1538-4357/ad66cf.
70. D. J. Eisenstein, *et al.*, Overview of the JWST Advanced Deep Extragalactic Survey (JADES). *arXiv e-prints* arXiv:2306.02465 (2023), doi:10.48550/arXiv.2306.02465.

71. K. E. Heintz, *et al.*, Strong damped Lyman- α absorption in young star-forming galaxies at redshifts 9 to 11. *Science* **384** (6698), 890–894 (2024), doi:10.1126/science.adj0343.
72. Z. Zhang, L. Jiang, W. Liu, L. C. Ho, K. Inayoshi, JWST Insights into Narrow-line Little Red Dots. *arXiv e-prints* arXiv:2506.04350 (2025), doi:10.48550/arXiv.2506.04350.
73. G. B. Brammer, P. G. van Dokkum, P. Coppi, EAZY: A Fast, Public Photometric Redshift Code. *Astrophys. J.* **686** (2), 1503–1513 (2008), doi:10.1086/591786.
74. M. J. Rieke, *et al.*, JADES Initial Data Release for the Hubble Ultra Deep Field: Revealing the Faint Infrared Sky with Deep JWST NIRCам Imaging. *Astrophys. J. Suppl. Ser.* **269** (1), 16 (2023), doi:10.3847/1538-4365/acf44d.
75. K. N. Hainline, *et al.*, The Cosmos in Its Infancy: JADES Galaxy Candidates at $z > 8$ in GOODS-S and GOODS-N. *Astrophys. J.* **964** (1), 71 (2024), doi:10.3847/1538-4357/ad1ee4.
76. B. Wang, *et al.*, Inferring More from Less: Prospector as a Photometric Redshift Engine in the Era of JWST. *Astrophys. J. Lett.* **944** (2), L58 (2023), doi:10.3847/2041-8213/acba99.
77. G. Bruzual, S. Charlot, Stellar population synthesis at the resolution of 2003. *Mon. Not. R. Astron. Soc.* **344** (4), 1000–1028 (2003), doi:10.1046/j.1365-8711.2003.06897.x.
78. G. Chabrier, Galactic Stellar and Substellar Initial Mass Function. *Publ. Astron. Soc. Pacific* **115** (809), 763–795 (2003), doi:10.1086/376392.
79. Y. C. Pei, Interstellar Dust from the Milky Way to the Magellanic Clouds. *Astrophys. J.* **395**, 130 (1992), doi:10.1086/171637.
80. D. Calzetti, *et al.*, The Dust Content and Opacity of Actively Star-forming Galaxies. *Astrophys. J.* **533** (2), 682–695 (2000), doi:10.1086/308692.
81. K. Chen, Z. Li, K. Inayoshi, L. C. Ho, Dust Budget Crisis in Little Red Dots. *arXiv e-prints* arXiv:2505.22600 (2025), doi:10.48550/arXiv.2505.22600.
82. D. J. Setton, *et al.*, A Confirmed Deficit of Hot and Cold Dust Emission in the Most Luminous Little Red Dots. *Astrophys. J. Lett.* **991** (1), L10 (2025), doi:10.3847/2041-8213/ade78b.

83. I. Soszyński, *et al.*, The OGLE Collection of Variable Stars. Classical Cepheids in the Magellanic System. *Acta Astronomica* **65** (4), 297–312 (2015), doi:10.48550/arXiv.1601.01318.
84. I. Soszyński, *et al.*, Concluding Henrietta Leavitt’s Work on Classical Cepheids in the Magellanic System and Other Updates of the OGLE Collection of Variable Stars. *Acta Astronomica* **67** (2), 103–113 (2017), doi:10.32023/0001-5237/67.2.1.
85. Y. Chen, *et al.*, YBC: a stellar bolometric corrections database with variable extinction coefficients. Application to PARSEC isochrones. *Astron. Astrophys.* **632**, A105 (2019), doi:10.1051/0004-6361/201936612.
86. J. Wambsganss, B. Paczynski, Expected Color Variations of the Gravitationally Microlensed QSO 2237+0305. *Astron. J.* **102**, 864 (1991), doi:10.1086/115916.
87. J. R. Gott, III, Are heavy halos made of low mass stars - A gravitational lens test. *Astrophys. J.* **243**, 140–146 (1981), doi:10.1086/158576.
88. M. R. S. Hawkins, The signature of primordial black holes in the dark matter halos of galaxies. *Astron. Astrophys.* **633**, A107 (2020), doi:10.1051/0004-6361/201936462.
89. P. Schneider, J. Ehlers, E. E. Falco, *Gravitational Lenses* (1992), doi:10.1007/978-3-662-03758-4.
90. L. Dai, T. Venumadhav, A. A. Kaurov, J. Miralda-Escud, Probing Dark Matter Subhalos in Galaxy Clusters Using Highly Magnified Stars. *Astrophys. J.* **867** (1), 24 (2018), doi:10.3847/1538-4357/aae478.
91. J. M. Diego, *et al.*, Imaging dark matter at the smallest scales with $z \approx 1$ lensed stars. *Astron. Astrophys.* **689**, A167 (2024), doi:10.1051/0004-6361/202450474.
92. S. Vegetti, L. V. E. Koopmans, M. W. Auger, T. Treu, A. S. Bolton, Inference of the cold dark matter substructure mass function at $z = 0.2$ using strong gravitational lenses. *Mon. Not. R. Astron. Soc.* **442** (3), 2017–2035 (2014), doi:10.1093/mnras/stu943.

93. J.-W. Hsueh, *et al.*, SHARP - VII. New constraints on the dark matter free-streaming properties and substructure abundance from gravitationally lensed quasars. *Mon. Not. R. Astron. Soc.* **492** (2), 3047–3059 (2020), doi:10.1093/mnras/stz3177.
94. D. Perera, *et al.*, Dents in the Mirror: A Novel Probe of Dark Matter Substructure in Galaxy Clusters from the Astrometric Asymmetry of Lensed Arcs. *arXiv e-prints* arXiv:2511.04748 (2025), doi:10.48550/arXiv.2511.04748.

Acknowledgments

The authors acknowledge the use of the Canadian Advanced Network for Astronomy Research (CANFAR) Science Platform operated by the Canadian Astronomy Data Center (CADC) and the Digital Research Alliance of Canada (DRAC), with support from the National Research Council of Canada (NRC), the Canadian Space Agency (CSA), CANARIE, and the Canadian Foundation for Innovation (CFI). This research is based on observations made with the NASA/ESA Hubble Space Telescope obtained from the Space Telescope Science Institute, which is operated by the Association of Universities for Research in Astronomy, Inc., under NASA contract NAS 5-26555. These observations are associated with program(s) GO-14096 (RELICS). This work is based on observations made with the NASA/ESA/CSA James Webb Space Telescope. The data were obtained from the Mikulski Archive for Space Telescopes at the Space Telescope Science Institute, which is operated by the Association of Universities for Research in Astronomy, Inc., under NASA contract NAS 5-03127 for JWST. These observations are associated with program #5594 (SLICE) and 6882 (VENUS). Some of the data presented herein were retrieved from the Dawn JWST Archive (DJA). DJA is an initiative of the Cosmic Dawn Center (DAWN), which is funded by the Danish National Research Foundation under grant DNR140. F.S. specially thank Dr. Roberto Decarli for hosting the Bologna meeting in 2025 summer that conceptualizes this project.

Funding: Z.Z. and L.J. acknowledge support from the National Science Foundation of China (12225301). M.O. acknowledges support from JSPS KAKENHI Grant Numbers JP25H00662, JP22K21349. K.I. acknowledges support from the National Natural Science Foundation of China (12573015, 1251101148, 12233001), the Beijing Natural Science Foundation (IS25003), and

the China Manned Space Program (CMS-CSST-2025-A09). J.M.D. acknowledges the support of projects PID2022-138896NB-C51 (MCIU/AEI/MINECO/FEDER, UE) Ministerio de Ciencia, Investigación y Universidades and SA101P24. R.A. acknowledges support of Grant PID2023-147386NB-I00 funded by MICIU/AEI/10.13039/501100011033 and by ERDF/EU, and the Severo Ochoa award to the IAA-CSIC CEX2021-001131-S. H.A. acknowledges support from CNES, focused on the JWST mission, and the French National Research Agency (ANR) under grant ANR-21-CE31-0838. P.D. warmly acknowledges support from an NSERC discovery grant (RGPIN-2025-06182). D.J.E. and J.A.A.T. acknowledge support from the Simons Foundation and JWST program 3215. D.J.E. was further supported by the JWST/NIRCam contract to the University of Arizona, NAS5-02015. G.E.M. acknowledges the Villum Fonden research grants 37440 and 13160. The Cosmic Dawn Center (DAWN) is funded by the Danish National Research Foundation under grant DNRF140. M.M. and E.V. acknowledge financial support through grants INAF GO Grant 2022 “The revolution is around the corner: JWST will probe globular cluster precursors and Population III stellar clusters at cosmic dawn”, INAF GO Grant 2024 “Mapping Star Cluster Feedback in a Galaxy 450 Myr after the Big Bang” and by the European Union - NextGenerationEU within PRIN 2022 project n.20229YBSAN - Globular clusters in cosmological simulations and lensed fields: from their birth to the present epoch. R.A.W. acknowledges support from NASA JWST Interdisciplinary Scientist grants NAG5-12460, NNX14AN10G and 80NSSC18K0200 from GSFC. A.Z. acknowledges support by the Israel Science Foundation Grant No. 864/23. F.S. acknowledge support from JWST program 4924 and 6434. Support for JWST program #3215, 4924, 5594, 6434 and 6882 was provided by NASA through a grant from the Space Telescope Science Institute, which is operated by the Association of Universities for Research in Astronomy, Inc., under NASA contract NAS 5-03127.

Author contributions: Z.Z. led the data analyses, physical interpretation, figure production and the paper writing. M.L. discovered the LRDs, contributed to the Keck data and figure production. M.O. led the multiple image identification and constructed the cluster mass model. X.L., K.I., F.S. contributed to the physical interpretation. Z.Z., M.L., X.L. and F.S. contributed to the JWST data processing. C.C, G.M. and K.S. led the JWST SLICE program design, data acquisition and contributed to the multiple image identification and cluster mass model. S.F. and D.C. led the JWST

VENUS program design and data acquisition. S.C., M.L., Y.L., N.R. and C.C.S. contributed to the Keck data. F.S. led the project conceptualization and administration. All authors contributed to the results, discussions and manuscript preparation.

Competing interests: The authors declare that they have no competing interests.

Data and materials availability: All JWST data and HST data are publicly available at MAST: <https://archive.stsci.edu/>. Image reduction and analysis used publicly available pipelines: CEERS NIRCcam (51), CIGALE (52, 53), GalfitM (54, 55), Source Extractor (56).

Supplementary materials

Materials and Methods

Supplementary Text

Figs. S1 to S9

Tables S1 to S2

References (51-94)

Supplementary Materials for

Little red dot variability over a century reveals black hole envelope via a giant Einstein cross

Zijian Zhang^{1,2}, Mingyu Li³, Masamune Oguri^{4,5}, Xiaojing Lin³, Kohei Inayoshi¹, Catherine Cerny⁶, Dan Coe^{7,8,9}, Jose M. Diego¹⁰, Seiji Fujimoto^{11,12}, Linhua Jiang^{1,2,*}, Guillaume Mahler¹³, Jorjyt Matthee¹⁴, Rohan P. Naidu¹⁵, Keren Sharon⁶, Yue Shen^{16,17}, Adi Zitrin¹⁸, Abdurro'uf¹⁹, Hollis Akins²⁰, Joseph F. V. Allingham¹⁸, Ricardo Amorín²¹, Yoshihisa Asada^{11,12}, Hakim Atek²², Franz E. Bauer²³, Maruša Bradač²⁴, Larry D. Bradley⁷, Zheng Cai³, Sebastiano Cantalupo²⁵, Christopher Conselice²⁶, Liang Dai²⁷, Pratika Dayal^{28,11,29}, Eiichi Egami³⁰, Daniel J. Eisenstein³¹, Andreas L. Faisst³², Xiaohui Fan³⁰, Qinyue Fei¹¹, Brenda L. Frye³⁰, Yoshinobu Fudamoto⁴, Lukas J. Furtak^{20,33}, Miriam Golubchik¹⁸, Mauro González-Otero²¹, Yuichi Harikane³⁴, Tiger Yu-Yang Hsiao^{20,33}, Yolanda Jiménez-Teja^{21,35}, Jeyhan S. Kartaltepe³⁶, Tomokazu Kiyota^{37,38}, Anton M. Koekemoer⁷, Kotaro Kohno^{39,40}, Vasily Kokorev^{20,33}, Nimisha Kumari⁹, Ivo Labbe⁴¹, Claudia D. P. Lagos^{42,43}, Conor Larison⁷, Yongming Liang^{34,38}, Ray A. Lucas⁷, Jianwei Lyu³⁰, Nicholas S. Martis²⁴, Georgios E. Magdis^{43,44}, Matteo Messa⁴⁵, Minami Nakane^{34,46}, Gaël Noirot⁷, Rafael Ortiz III⁴⁷, Masami Ouchi^{38,34,XX,48}, Justin D. R. Pierel⁷, Marc Postman⁷, Naveen Reddy⁴⁹, Massimo Ricotti⁵⁰, Daniel Schaerer^{51,52}, Raffaella Schneider⁵³, Charles C. Steidel⁵⁴, Wei Leong Tee⁵⁵, Roberta Tripodi^{56,24,57}, James A. A. Trussler³¹, Hiroya Umeda^{34,46}, Francesco Valentino^{43,44}, Eros Vanzella⁴⁵, Feige Wang⁶, Rogier Windhorst⁴⁷, Yunjing Wu³, Zihao Wu³¹, Hiroto Yanagisawa^{34,46}, Jinyi Yang⁶, Fengwu Sun^{31,*}

*Corresponding authors. Email: fengwu.sun@cfa.harvard.edu (Fengwu Sun) & jiangKIAA@pku.edu.cn

(Linhua Jiang)

This PDF file includes:

Materials and Methods

Supplementary Text

Figures S1 to S9

Tables S1 to S2

Materials and Methods

Imaging Data and Photometry

In this work, we use the JWST/NIRCam data taken by the Vast Exploration for Nascent, Unexplored Sources (VENUS) program (PID: 6882; PI: Fujimoto) and Strong LensIng and Cluster Evolution (SLICE) program (29) (PID: 5594; PI: Mahler). The VENUS program is designed to deliver uniform ten-band NIRCam imaging across $0.8\text{--}5.0\ \mu\text{m}$ for a sample of 60 massive and well-studied galaxy clusters. As part of this survey, RXC J2211–0350 was observed in ten NIRCam filters: F090W, F115W, F150W, F200W, F210M, F277W, F300M, F356W, F410M, and F444W on UT October 16, 2025. The SLICE program obtained NIRCam imaging of RXC J2211–0350 in the ultra-wide F150W2 and F322W2 bands on UT November 17, 2024. We also include archival HST/ACS imaging data in the F435W, F606W, and F814W bands from the Reionization Lensing Cluster Survey (57) (RELICS) for part of our analyses.

All NIRCam imaging data were uniformly processed using a customized JWST pipeline¹ (58) (v1.18.0) and CRDS context map `jwst_1364.pmap`. The customized steps include: (i) $1/f$ noise stripe removal in both row and column directions; (ii) wisp removal in the NIRCam short-wavelength (SW) detectors using STScI-provided templates; (iii) bad-pixel masking based on sigma-clipped median images from each detector; (iv) median sky-background subtraction; and (v) world coordinate system (WCS) correction using the DESI Legacy Imaging Survey (59) DR10 source catalog, which is tied to the Gaia DR2 astrometric reference frame (60). Calibrated NIRCam images in each band were mosaicked through a standard stage-3 pipeline with an output pixel size of $0''.03$, `pixfrac` = 1.0 and a common north-up-east-left WCS frame for all filters. The diffuse intracluster light (ICL) is not subtracted from the images.

Following methods in previous work (61), we create a stacked NIRCam detection image combining the F200W–F444W bands to optimize the S/N and apply iterative image sharpening to improve source deblending in the crowded cluster field. Source detection and photometric measurements are then performed using a customized `photutils` pipeline (62). We perform aperture photometry on NIRCam-detected sources using a range of aperture radii from $0''.1$ to $0''.5$ as well as Kron apertures, with local background measured through rectangular annuli and subtracted. Aperture losses

¹<https://github.com/spacetelescope/jwst>

are corrected using empirical PSF models constructed from stacks of ~ 10 bright, isolated stars within the imaging footprint. Photometric uncertainties are estimated from both error extensions and random-aperture experiments, adopting the larger of the two as the final error. The median 5σ depth for point sources measured with an $r = 0''.1$ aperture is 28.0 ± 0.1 mag (28.3 ± 0.2 mag) in the five VENUS NIRCcam band in the SW (LW) channel, respectively. For the SLICE F150W2 and F322W2 bands, the corresponding depth is 28.8 mag.

Since all images of R2211-RX1 are perfect point sources, for this source we use the simple aperture photometry with $r = 0''.15$ and aperture correction to improve S/N. For R2211-RX2.2, R2211-RX2.3, and R2211-RX2.4, we also use the above photometry. R2211-RX2.1, however, has a nearby companion that is not physically associated, as inferred from the prior of its other images, the z_{phot} , and magnification values. We therefore fit R2211-RX2.1 and this companion with a central PSF and an offset Sérsic model simultaneously using GALFITM and adopt the best-fit PSF model as its final photometry. For R2211-RX2.5, it has a significant off-centered extended component. Its elongation direction is aligned with the direction of μ_{tan} . The large tangential magnification and consistent photometric redshift also support that the extended component is physically associated with R2211-RX2.5. We therefore fit it using a PSF+Sérsic model and adopt the sum of these two components as its final photometry. Both R2211-RX2.1 and R2211-RX2.2 suffer from strong intracluster light (ICL), which biases the fitting. Before running GALFITM, we therefore subtract a smooth 2D background using a median-based estimator and Gaussian filtering (via Background2D), ensuring that the PSF+Sérsic modeling is not affected by large-scale ICL residuals. Photometry of R2211-RX1 and R2211-RX2 are presented in Table S1.

Strong Lens Mass Modeling

We use glafic (30, 31) to construct a strong lens mass model of RXC J2211–0350. For this cluster, 3 multiply imaged sources are reported previously (63) and 6 more multiply imaged sources are reported in later work (29). We search for multiple images in the VENUS data to identify additional 34 multiply imaged sources. In practice, multiple images are discovered iteratively based on their similar morphologies, colors, photometric redshifts and consistency with the predicted image-plane positions from the previous best cluster mass model. In total, we use 146 multiple images from 43 sources for the mass modeling, which are summarized in Figure S3 and Table S2. The spectroscopic

redshift of one of the sources is reported in previous work (63), and spectroscopic redshifts for two additional sources are obtained from our recent Keck/KCWI observation (private communication from Sebastiano Cantalupo, Mingyu Li et al.). When accurate photometric redshifts are available, we include Gaussian priors on their redshifts, typically assuming the width of $\sigma_z = 0.2$ according to the photometric redshift posteriors. For R2211-RX1 and R2211-RX2, we adopt a conservative Gaussian prior to their redshift of 4.3 ± 0.4 (See Photometric Redshift section). We fit the multiple image positions assuming two halo components modeled by the elliptical density profile (64), member galaxies modeled by the pseudo-Jaffe ellipsoids, external shear, and third and fourth order multipole perturbations (see e.g., (65) for more detailed explanations of these lens components).

Assuming the positional error of 0''.6 (but 0''.2 for a few close pairs of multiple images), our best-fitting mass model has $\chi^2 = 174.5$ for the degree of freedom of 180. The root-mean-square between observed and model-predicted multiple image positions is 0''.61. Figure S3 indicates that there are many other multiple images near each multiple image of R2211-RX1 and R2211-RX2, implying that their magnifications and time delays are tightly constrained by the mass modeling. Errors on model parameters are obtained by the Markov chain Monte Carlo (MCMC).

We use the cluster mass model to examine the redshift of the source. We systematically test a grid of candidate source redshifts spanning 0 to 10. For each assumed redshift, we use the cluster mass model to inverse-map all observed multiple images of the source back to the source plane. A valid redshift should produce a consistent source plane position for all the images. Using this method, our model strongly suggest that the redshifts of R2211-RX1 and R2211-RX2 are in the range of 4-5.5, which is consistent with our z_{phot} estimation.

Construction of Empirical LRD Templates

As LRDs are a newly identified population not represented in current photometric redshift template libraries, such mismatch can bias the photometric redshift estimates. Therefore, we construct empirical LRD templates based on the JWST/NIRSpec prism spectra of 44 confirmed LRDs at $z = 2.3-7$. These LRD spectra are mainly collected from previous work (66, 67), primarily originating from the RUBIES (68), UNCOVER (69), and JADES (70) programs. We also include several well studied LRDs (11, 12, 14, 24). Their NIRSpec spectra are from the DAWN JWST

Archive (DJA²). We use the version 4 publicly released NIRSpec datasets. These data are reduced using the latest version of `msaexp` and the *JWST Calibration Pipeline* (68, 71). The spectroscopic redshifts are obtained through the template fitting algorithms employed in the `msaexp` pipeline.

To construct a representative empirical template, we first shifted all LRD spectra to the rest frame and interpolated them onto a common logarithmic wavelength grid between 0.7 and 2.5 μm . Each spectrum was normalized at 5500 Å. To suppress noisy data in the blue end, we identified regions with $S/N < 3$ shortward of the Lyman limit (912 Å) and masked those pixels. We first obtain a full-sample composite spectrum of all objects by taking the sigma-clipped (3σ) median of all fluxes at each wavelength, followed by a mild boxcar smoothing below 1216 Å to mitigate residual noise. The resulting composite spectrum cover a wide redshift range thanks to the wide redshift range of the sample.

To capture the observed diversity in LRD continua, we further divided the sample in the $(\beta_{\text{UV}}, \beta_{\text{opt}})$ plane as shown in Figure S5(A), where β_{UV} and β_{opt} were measured from line-free photometry (72). We adopted bin edges of $\beta_{\text{UV}} = [-2.0, -1.0]$ and $\beta_{\text{opt}} = [-0.65, 0, 0.5, 1.4]$, yielding twelve subsamples with distinct UV-optical slopes. Each subsample typically contained 2-7 LRDs. For each bin, we repeated the same stacking procedure above. Because many individual spectra have limited wavelength coverage or low S/N in the rest-frame far-UV, we further patched each subsample’s median stack using the full-sample composite. Specifically, pixels below 2000 Å with $S/N < 1$ or missing data were replaced by the full-sample template, scaled to match the median flux around 2500 Å. Typically this replacement occurs near/blueward the Lyman-break. This approach preserves each group’s overall continuum slope while ensuring smooth, noise-free behavior around the Lyman-break region.

These twelve empirical templates, together with the global median composite are shown in Figure S5(B). They provide a flexible basis set for EAZY z_{phot} estimation, allowing the continuum slope and Balmer break strength to vary smoothly. The resulting library effectively captures the observed diversity of LRDs across UV-optical colors while maintaining realistic spectral shapes at all wavelengths. The library is available at <https://github.com/Zijian-astro/LRD-template-Zhang25>.

²<https://dawn-cph.github.io/dja/>.

Photometric Redshift

We first use `EAZY` (73) to measure photometric redshifts of all sources in the RXC J2211–0350 field, following a similar method to that adopted by the JADES team (74, 75). We include ten NIRCcam bands from the VENUS survey. We use photometry with aperture of $r = 0''.15$ and impose a minimum uncertainty of 5% on the flux for `EAZY` SED fitting. The spectral template set from (75) is adopted. We adopt the `EAZY` error template `TEMPLATE_ERROR.v2.0.zfourge` to account for wavelength-dependent uncertainties in the templates. We explore a redshift range of $z = 0.01$ –30 with a step size of $\Delta z = 0.01$, adopting the redshift corresponding to the global minimum of $\chi^2(z)$ as our best-fit z_{phot} . The output probability distribution $P(z) \propto \exp[-\chi^2(z)/2]$ is used to estimate the z_{phot} uncertainties. Although the redshift grid formally extends to $z = 30$, the multiply imaged sources considered here are mostly to lie at $z \lesssim 7$ (Table S2), where Ly α -damping and DLA absorption have minimal impact on the NIRCcam SEDs. Therefore, the adopted template set from (75) is sufficient for our analysis.

For both R2211-RX1 and R2211-RX2, the initial z_{phot} estimates of the multiple images show two degenerate redshift peaks around $z \sim 4.3$ and $z \sim 6.3$. To further improve the constraints, we include the HST F435W, F606W, and F814W bands. The HST measurements of the individual images are all upper limits, which are estimated from random-aperture experiments. To enhance the overall constraint, we perform z_{phot} fitting on the stacked photometry of the multiple images, since stacking improves the S/N in the relatively faint bands. For R2211-RX1, we stack all four images, whereas for R2211-RX2 we stack only the three brightest ones (2.3, 2.4, and 2.5). We obtain photometry with radius of $0''.15$ and aperture correction. Another source of z_{phot} uncertainty arises from the mismatch between the observed SEDs of LRDs and the galaxy templates used in the fitting. We thus apply the LRD templates constructed above to the stacked photometry using `EAZY`. To assess z_{phot} uncertainty, we also fit the stacked SED of R2211-RX1 and R2211-RX2 using two additional SED fitting codes, `PROSPECTOR` (76) and `CIGALE` (52, 53). The `PROSPECTOR` setup follows those in previous work (76), and the `CIGALE` setup are detailed below.

The SEDs, best-fit z_{phot} results, and image cutouts of R2211-RX1 and R2211-RX2 are shown in Figure S1. The stacked images of both R2211-RX1 and R2211-RX2 show a $\sim 3\sigma$ detection in the F814W band, while F435W and F606W remain undetected. The `EAZY` fitting using the empirical

LRD templates obtain $z_{\text{phot}} = 4.53^{+0.09}_{-0.16}$ for R2211-RX1 and $z_{\text{phot}} = 4.10^{+0.59}_{-0.19}$ for R2211-RX2. These values are slightly lower than those derived using galaxy templates with EAZY, CIGALE, and PROSPECTOR. The primary constraints arise from the combination of significant flux excesses in the F277W and F356W bands (relative to F210M, F300M, and F410M) and the non-detections in the F435W and F606W bands, together indicating a redshift in the range $z \approx 3.9\text{--}4.7$. It is insufficient to provide tighter constraints within this redshift range based on the photometric data alone. Notably, both LRDs are located in a region associated with a potential galaxy overdensity (Figure S4). Considering the z_{phot} of nearby member galaxies, we estimate the most probable redshift of this structure to be $z \sim 4.3$, and therefore adopt $z = 4.3$ as the fiducial redshift for R2211-RX1 and R2211-RX2. We note that adopting any redshift within $z = 3.9\text{--}4.7$ would not affect the conclusions of this work.

CIGALE SED modeling setup

For CIGALE SED modeling, we assume a delayed- τ star formation history (SFH), where $\text{SFR} \propto te^{-t/\tau}$ and $\tau \in [0.01, 2]$ Gyr. We also allow an optional late starburst in the latest 20 Myr. We use the (77) stellar population synthesis models and adopt the (78) initial mass function (IMF). Nebular continuum and emission lines are included, allowing a metallicity range of $[0.2, 1] Z_{\odot}$ and an ionization parameter $\log U \in [-4, -1]$. We adopt the SMC extinction curve (79) for nebular emission and the modified (80) attenuation curve for the stellar continuum, with the power-law slope $n \in [-0.6, 0.2]$. We add a relative error of 5% in quadrature to the uncertainties of the fluxes.

V-shape Continua and Compactness

Using the estimated photometric redshift, we derive the rest-frame UV and optical slopes of R2211-RX1 and R2211-RX2, excluding the F277W and F356W bands where strong emission-line contamination from [O III]+H β and H α is expected. Figure S2(A) shows their locations in the $\beta_{\text{UV}}\text{--}\beta_{\text{opt}}$ plane. The scatter in positions of the different images of the same source reflects both the large uncertainties in the rest-frame UV measurements and potential variability. According to the commonly adopted V-shape criterion of $\beta_{\text{opt}} > 0$ and $\beta_{\text{UV}} < -0.37$ (4), R2211-RX1 clearly qualifies as an LRD. Although R2211-RX2 has a slightly smaller β_{opt} and thus falls slightly outside the canonical boundary, it remains on the red side of the distribution. We overlay in Figure S2(A) the

empirical relation between the UV/optical slopes and the fraction of broad $H\alpha$ emitters from (72). The position of R2211-RX2 strongly suggests that it has broad lines.

To demonstrate their compact morphologies, we show the relation between m_{F444W} and R_{F444W} in Figure S2(B). We derive a relation between m_{F444W} and R_{F444W} for point sources as a green line by fitting the stellar locus. Both R2211-RX1 and R2211-RX2 have radii smaller than 1.5 times this relation, confirming their point-like morphologies in the F444W band. Taken together, their V-shaped continua and compact morphologies qualify both objects as LRDs, awaiting further spectroscopic confirmation.

Blackbody SED Fitting

To investigate the physical origin of the observed coupling between color and luminosity variability of R2211-RX1, we model the SEDs of R2211-RX1 at each epoch using a single-temperature blackbody component following recent studies (18, 19, 35, 37). To account for the potential host galaxy dominated in the rest-frame UV, we add a power-law component. Its normalization and slope are shared across all epochs but remain free parameters in the fit. The F277W and F356W bands are excluded from the fit because they are strongly contaminated by emission lines. The blackbody temperature is degenerate with the dust extinction level, as illustrated in Figure 5 of (18). However, only mild dust extinction is expected for LRDs (19, 81, 82). Therefore, we do not consider dust attenuation in our fitting. This simple model provides a reasonable fit to the SEDs of R2211-RX1 (Figure 3A), with $T_{\text{eff}} \sim 4000$ K, $R_{\text{ph}} \sim 2000$ AU, and $L_{\text{BB}} \sim 2 \times 10^{44} \text{ erg s}^{-1}$. We also fit the SED of R2211-RX2 using the same model, obtaining $T_{\text{eff}} \sim 5000$ K, $R_{\text{ph}} \sim 600$ AU, and $L_{\text{BB}} \sim 2 \times 10^{43} \text{ erg s}^{-1}$. The final L_{BB} used as the bolometric luminosity of R2211-RX1 and R2211-RX2 are the mean L_{BB} of all epoch, with the error obtained by MC sampling. We also try to include dust attenuation using the Calzetti dust extinction law (80) with different A_V for the blackbody. Altering the A_V value in the range of 0-2 would change the fitted blackbody temperature in the range of 3500-6000 K, but does not change the main conclusions of this work.

Light Curve Fitting

Previous studies suggest that supermassive stars are unstable only under radial perturbations (42, 45). By analogy, we consider only the f-mode for LRDs, which is expected to dominate their pulsational

instability. In this case, the characteristic pulsation period of the LRD envelope is expected to be $T_0 = f_0 t_{\text{dyn}}$, where we adopt $f_0 = 0.37$ assuming an $n = 3$ polytropic equation of state (fully convective, radiation-pressure dominated envelopes) (46). Using the inferred properties of R2211-RX1 (i.e., $T_{\text{eff}} = 4000$ K and $M_{\text{BH}} = 10^{6.28} M_{\odot}$), we calculate the pulsation period as

$$T_0 \approx 32 \text{ yr} \lambda_{\text{Edd}}^{3/4} \left(\frac{f_0}{0.37} \right) \left(\frac{M_{\text{BH}}}{10^{6.28} M_{\odot}} \right)^{1/4} \left(\frac{T_{\text{eff}}}{4000 \text{ K}} \right)^{-3}. \quad (\text{S1})$$

The variability in each band is then modeled as a single shared-phase sinusoid

$$f(t) = \bar{f} + A_0 \sin \left(\frac{t}{T_0} + \phi_0 \right), \quad (\text{S2})$$

where \bar{f} is the mean flux, A_0 is the variability amplitude, and ϕ_0 is the common oscillation phase across all fitted bands. We fit this model to the R2211-RX1 light curves for bands longer than F210M. For the F322W2 band from SLICE, we additionally include the synthetic mean fluxes of the VENUS F277W and F356W bands, since F322W2 is equivalent to the combination of these two bands. We fit six bands simultaneously, each band containing four independent epochs, so the total $N_{\text{data}} = 6 \times 4 = 24$ measurements. The model has two free parameters (mean flux \bar{f}_i and amplitude A_i) for each band (12 parameters total) plus a single global phase ϕ tied across all bands. Hence the total number of fitted parameters is $N_{\text{par}} = 2 \times 6 + 1 = 13$, giving $\text{dof} = N_{\text{data}} - N_{\text{par}} = 24 - 13 = 11$. All bands are well fitted by this model, with a total $\chi^2_{\nu} = 0.09$.

To map the regions of parameter space that yield reasonable fit to the observed data, we perform a grid search over the black hole mass and effective temperature. We evaluate a two-dimensional grid spanning $\log(M_{\text{BH}}/M_{\odot}) \in [4, 9]$ and $T_{\text{eff}} \in [3000, 6000]$ K, with 500 uniformly spaced samples in each dimension. For each grid point, the corresponding pulsation period T_0 is computed, and this fixed period is adopted in the multi-band sinusoidal model. At every $(M_{\text{BH}}, T_{\text{eff}})$, we refit the full set of six bands simultaneously using the same procedure described above. The final χ^2_{ν} map is shown in Figure S8. Only a narrow strip in the $M_{\text{BH}}-T_{\text{eff}}$ plane yields comparably good fits, forming the valley of low χ^2_{ν} values that identifies the reasonable pulsation periods. The independently inferred parameters of R2211-RX1 lie precisely within this region, demonstrating that the fit is physically self-consistent rather than an artifact of flexible modeling.

We note that with the current sparse sampling, smaller-timescale variability could still be present (there are some very narrow low χ^2_{ν} valley in the upper-right corner of Figure S8). Nevertheless, prior

observations shows that LRDs do not exhibit strong variability on rest-frame ~ 1 -year timescales (23), and the VENUS-SLICE observed one-year baseline shows no significant flux changes (Figure S7). Furthermore, shorter pulsation periods of only a few years would imply implausibly low LRD black hole masses of $< 10^4 M_{\odot}$, reinforcing the plausibility of the multi-year characteristic timescale implied by our best-fit model.

Using the best-fit light curve models, we sample 40 epochs at one-year intervals and fit each epoch with the same blackbody+power-law model as in Figure 3(A). This yields the temporal sequence of luminosity and temperature variations, which is shown in Figure 3(B).

Cepheid Temperature and Luminosity Evolution

To illustrate the similarity between the observed variability of R2211-RX1 and the κ -mechanism-driven pulsations of Cepheid-like stars, we compare their behaviors in the luminosity–temperature ($T_{\text{eff}}-L_{\text{BB}}$) plane. We retrieve observed light curve of Cepheids from the OGLE Collection of Variable Stars (83, 84), which is the largest set of variable stars and provides well-sampled V - and I -band light curves of ~ 5000 classical Cepheids. For each source, we fold the light curves with the published period and construct smooth phase-dependent V and I magnitudes using a spline fit because the V and I data points are usually not observed simultaneously. The color curve is then converted to T_{eff} through interpolation of the bolometric correction obtained from YBC, a stellar bolometric corrections database³ (85). The L_{BB} is also derived from the corresponding bolometric corrections from YBC and normalized to its cycle-averaged value.

This procedure yields a closed trajectory in the $T_{\text{eff}}-L_{\text{BB}}$ plane for every Cepheid. As shown in Figure S9, the track of a representative Cepheid (OGLE-LMC-CEP-4313) exhibits a characteristic counterclockwise loop: the temperature rises rapidly near maximum compression, reaches its peak slightly before luminosity maximum, and then decreases gradually during the expansion phase. The phase offset between luminosity and temperature extrema, which results in the counterclockwise trajectory in the $T_{\text{eff}}-L_{\text{BB}}$ plane, is a hallmark of κ -mechanism pulsation and is also seen in the variability pattern of R2211-RX1 (Figure 3b).

³<https://sec.center/YBC/>.

Supplementary Text

Cluster Mass Model and Magnification Uncertainty

The main source of uncertainty for this lensing variability study arises from systematic errors in the lensing magnification. We note that our cluster mass model is constructed using a large number of multiple images, three of which have spectroscopic redshifts. All images of R2211-RX1 are considerably far away from the critical curve ($\gtrsim 15''$), and therefore the magnification uncertainty from the cluster mass model is estimated to be small ($\sigma_\mu/\mu \lesssim 0.05$; see Strong Lens Mass Modeling section). Given the large distance and compact size of LRDs, we also estimate a negligible uncertainty in color variation attributed to differential lensing magnification ($\sigma_\mu/\mu \lesssim 0.003$), unlike the color variation observed in galaxy-lensed quasars (86).

To further assess potential systematic cluster-lensing uncertainty propagated to the variability signal, we compare R2211-RX1 with 12 other multiply imaged sources that have $z_{\text{phot}} > 3$ in the same field. Among them, six have similar redshift of R2211-RX1 and R2211-RX2, as shown in Figure S4. Several of these sources lie very close to R2211-RX1 in the source plane and should have similar light path (e.g., ID16 and ID37). For each source, we compute the S/N of the de-magnified magnitude difference (i.e., $|\Delta\text{mag}/\sigma_{\Delta\text{mag}}|$) between all epoch pairs in the F200W and longer-wavelength bands. $\sigma_{\Delta\text{mag}}$ is the quadrature sum of the magnitude uncertainties of the two epochs, including both the measurement errors and the uncertainties in the lensing magnification. The median of these band-wise S/N values is adopted as the variability S/N for the epoch pair, which is designed to quantify the overall SED variability. Similarly, we calculate the color (F300M–F444W) variability S/N for each epoch pair. This provides a measure of changes in the spectral shape independent of the overall brightness. As shown in Figure 2(C), the distribution of the magnitude and color variability S/N for the other sources is predominantly below unity, whereas R2211-RX1 shows a clear excess and reaches > 3 . The lack of significant variability in the comparison sample confirms that the observed flux variability in R2211-RX1 should be intrinsic, rather than caused by the systematic uncertainties of cluster magnification model. The non-detection of variability in the SW bands of R2211-RX1 and LW bands of R2211-RX2 further supports the reliability of their magnification corrections.

In addition, we assess whether microlensing could contribute to the observed variability (e.g.,

(87)). We estimate the expected microlensing optical depth from the stellar surface mass density of the cluster. The stellar convergence κ_* is derived from the observed surface brightness profile of the cluster at the F210M band (corresponds to rest-frame H-band), scaled by a mass-to-light ratio of $M/L_H = 0.57 \pm 0.26$ (88), and compared to the total convergence κ_{tot} from the cluster mass model. The optical depth is expressed as (89)

$$\tau = \frac{\kappa_*}{1 - \kappa_c} \quad (\tau \lesssim 0.1, \kappa_c < 1), \quad (\text{S3})$$

where $\kappa_c = \kappa_{\text{tot}} - \kappa_*$ represents the convergence of the smoothly distributed matter. This value quantifies the probability that light rays from the source are significantly perturbed by compact stellar lenses. For the positions of R2211-RX1.1 and R2211-RX1.2, we find $\kappa_{\text{tot}} \sim 0.5$, $\kappa_* < 5 \times 10^{-4}$, and $\tau < 1 \times 10^{-3}$, implying that the possibility of a microlensing event is negligible. Notably, R2211-RX1.1 and R2211-RX1.2 correspond to the brightest and dimmest images, respectively. For R2211-RX1.3 and R2211-RX1.4, where $\kappa_c \sim 1.3$, the optical-depth expression is not strictly valid, but given their similarly small κ_* , the probability of microlensing remains extremely low. Moreover, even if rare microlensing events occur, it would be in the finite-source regime. For a typical stellar lens, an Einstein radius of $\Theta_E \sim 1 \mu\text{as}$ corresponds to ~ 1000 AU at $z \simeq 4.3$, while the source size inferred from our blackbody fit is ~ 2000 AU. Taking a typical transverse velocity of $v \sim 1000 \text{ km s}^{-1}$ from the cluster velocity dispersion, the corresponding crossing time of ~ 4.7 yr would make microlensing-induced variability evolve measurably over the JWST mission lifetime. In fact, the F150W2 and F322W2 photometry obtained in 2024 agrees well with the 2025 measurements at similar wavelengths for all four images, further suggesting that microlensing is unlikely to be responsible for the observed variability.

We also assess whether “millilenses”, such as globular clusters or dark matter subhalos with masses $M \simeq 10^6 - 10^9 M_\odot$ (corresponding to Einstein radii $\Theta_E \simeq 0.001 - 0.1''$), could contribute to the observed brightnesses variation with a characteristic timescale of a few hundred years in the observed frame (90, 91). Such perturbers would introduce differential magnification across the source, potentially producing color differences among the multiple images of lensed LRDs. In particular, if the LRD is more compact in the rest-frame optical than in the UV, millilensing would induce larger brightness changes at optical wavelengths. At the depth of VENUS imaging, we are able to rule out the presence of dwarf galaxy or massive globular cluster with luminosities

$L \gtrsim 2 \times 10^7 L_{\odot}$ along the sightlines of LRD images. Below this detection limit, (91) shows that globular clusters in the galaxy cluster only contribute to $\sim 10^{-2} - 10^{-1}$ of the microlensing cross sections above a given magnification, and thus can be ruled out. On the other hand, the mass fraction of dark matter subhalo at $M \lesssim 10^9 M_{\odot}$ is typically constrained as $f_{\text{sub}} \lesssim 10^{-2}$ in low-redshift strong gravitational lenses (92–94). The optical depth of subhalo millilens follows similar formalism as that of microlenses (Equation S3) and thus $\tau \sim f_{\text{sub}} \lesssim 10^{-2}$. Therefore, we conclude that millilenses are unlikely the main cause of the observed brightness and color variation seen in the multiple images of R2211-RX1.

Other uncertainties of the variability measurement arise from variations in depth, spatial PSF, statistical noise, and contamination from nearby sources, etc. These effects lead to scatter among non-variable sources (23). We carefully inspected the image cutouts for every band and for every image: in all cases the sources are isolated, there is no evidence of flux contamination from nearby objects, and the local background and PSF structure do not show anomalies that could bias the aperture photometry. Crucially, the variability follows the same trend across all bands. Random measurement fluctuations or intermittent contamination (e.g., cosmic rays or hot pixels) in individual images would produce uncorrelated or band-dependent behavior, yet we observe coherent variability even between datasets taken at different epochs and under different configurations from SLICE and VENUS. We therefore conclude that the variability signals are genuine.

Table S1: Photometry of the multiple images of R2211-RX1 and R2211-RX2. Fluxes in the units of nJy are measured from the HST (RELICS program) and JWST/NIRCam (VENUS and SLICES programs) imaging. Photometry is not corrected for lensing magnification. For R2211-RX1 and R2211-RX2.3-5, we use the simple aperture photometry with $r = 0''.15$ and apply the aperture correction. The flux of R2211-RX2.1 and R2211-RX2.2 are measured using GALFITM with a PSF+Sérsic model. For bands in which the images are not detected, we list the 2σ upper limits.

ID	F435W	F606W	F814W	F090W	F115W	F150W	F150W2	F200W
R2211-RX1.1	< 33	< 17	< 25	28 ± 4	34 ± 4	57 ± 5	66 ± 3	84 ± 4
R2211-RX1.2	< 31	< 15	< 25	16 ± 3	18 ± 4	22 ± 4	25 ± 2	42 ± 3
R2211-RX1.3	< 32	< 14	< 24	12 ± 4	26 ± 4	29 ± 5	35 ± 2	47 ± 4
R2211-RX1.4	< 52	< 20	< 40	24 ± 4	27 ± 4	46 ± 4	45 ± 2	61 ± 4
R2211-RX1 (stack)	< 15	< 8	24 ± 7	20 ± 2	26 ± 2	37 ± 2	37 ± 2	56 ± 3
R2211-RX2.1	< 56	< 21	< 40	9 ± 3	8 ± 3	6 ± 2	6 ± 2	9 ± 2
R2211-RX2.2	< 28	< 15	< 22	< 10	< 12	< 12	< 6	< 10
R2211-RX2.3	< 29	< 13	< 23	19 ± 4	13 ± 4	20 ± 4	17 ± 2	19 ± 4
R2211-RX2.4	< 32	< 14	< 24	7 ± 3	12 ± 4	16 ± 4	15 ± 2	26 ± 3
R2211-RX2.5	< 34	< 15	< 26	17 ± 3	14 ± 4	26 ± 4	28 ± 2	39 ± 4
R2211-RX2 (stack)	< 17	< 8	28 ± 7	18 ± 2	14 ± 3	23 ± 3	24 ± 2	29 ± 3
ID	F210M	F277W	F300M	F322W2	F356W	F410W	F444W	
R2211-RX1.1	94 ± 5	409 ± 20	417 ± 21	681 ± 34	966 ± 48	794 ± 40	897 ± 45	
R2211-RX1.2	45 ± 4	140 ± 7	132 ± 7	253 ± 13	362 ± 18	303 ± 15	328 ± 16	
R2211-RX1.3	58 ± 5	205 ± 10	205 ± 10	360 ± 18	524 ± 26	412 ± 21	451 ± 23	
R2211-RX1.4	74 ± 5	260 ± 13	258 ± 13	437 ± 22	638 ± 32	516 ± 26	575 ± 29	
R2211-RX1 (stack)	65 ± 3	192 ± 10	183 ± 9	341 ± 17	491 ± 25	403 ± 20	440 ± 22	
R2211-RX2.1	8 ± 2	19 ± 4	6 ± 2	30 ± 2	36 ± 2	21 ± 2	19 ± 2	
R2211-RX2.2	< 10	24 ± 2	8 ± 2	21 ± 2	30 ± 2	23 ± 2	21 ± 2	
R2211-RX2.3	14 ± 4	49 ± 3	36 ± 4	70 ± 4	89 ± 4	60 ± 4	60 ± 4	
R2211-RX2.4	18 ± 4	56 ± 3	39 ± 4	74 ± 4	95 ± 5	56 ± 4	62 ± 4	
R2211-RX2.5	38 ± 4	109 ± 5	80 ± 4	150 ± 7	197 ± 10	135 ± 7	149 ± 7	
R2211-RX2 (stack)	26 ± 3	64 ± 3	56 ± 3	84 ± 4	107 ± 5	81 ± 4	79 ± 4	

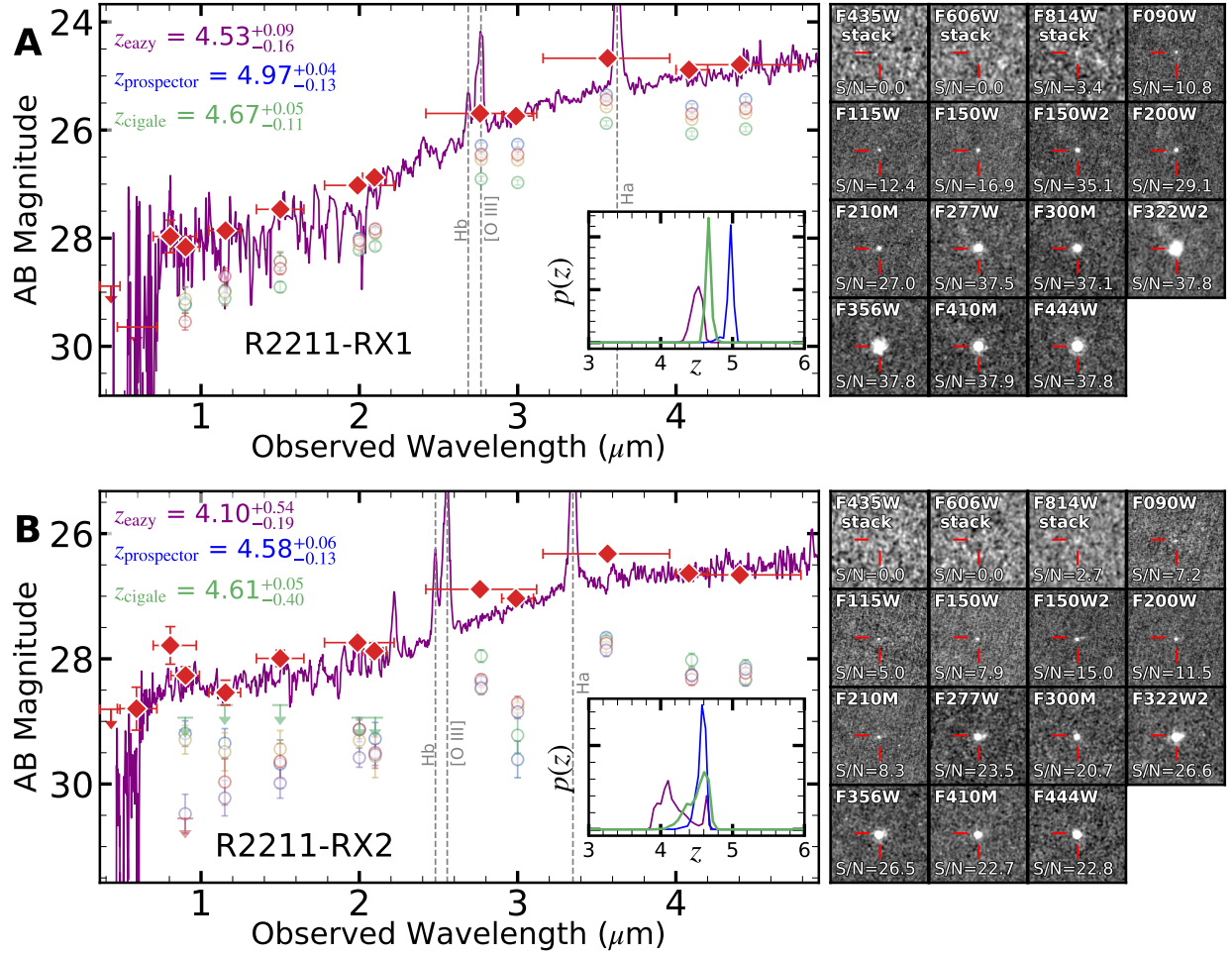


Figure S1: The SED and images of R2211-RX1 (A) and R2211-RX2 (B). The left panels show the stacked observed photometry and 2σ upper limits from VENUS JWST bands and RELICS HST F435W/F606W/F814W data (dark red diamonds). The best-match LRD template is overplotted in purple, and the best-fit redshifts (z_{map}) with their 5th-95th percentile ranges from EAZY, CIGALE, and Prospector are indicated. The photometry from individual images (corrected for magnification μ) is shown as lighter/semi-transparent markers in the background. The inset panels display the full redshift probability distributions $p(z)$ from the same three codes. The right panels show $3'' \times 3''$ cutouts in the available JWST bands of R2211-RX1.4 and R2211-RX2.5, as well as the stacked HST F435W/F606W/F814W images. We show these two images because they have high magnifications and no nearby contamination. For R2211-RX1, the HST stack combines all multiple lensed images of the same source, while for R2211-RX2, the stack includes only images R2211-RX2.3, R2211-RX2.4, and R2211-RX2.5. The HST stacked images are smoothed with a Gaussian kernel ($\sigma = 1$ pixel).

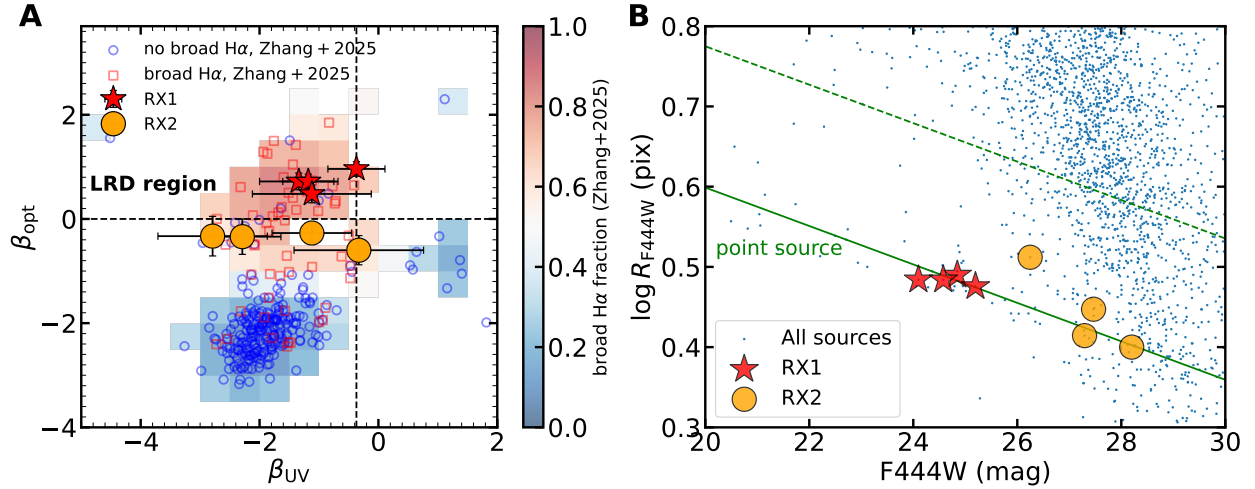


Figure S2: The colors, sizes and magnitudes of R2211-RX1 and R2211-RX2 as LRDs. (A) Distribution of the best-fit UV and optical slope using the line-free photometry for R2211-RX1 and R2211-RX2. Dashed lines represent the LRD selection criteria (upper left region) (4). The color of the background squares represents the fraction of broad-line sources adopted from (72). The red squares and blue circles represent sources with and without broad H α lines in (72). **(B)** F444W magnitude versus half-light radius diagram. Green solid and dashed lines denote the best-fit relation to the stellar locus and 1.5 times this relation. Blue dots in the background show all sources in RXC J2211–0350.

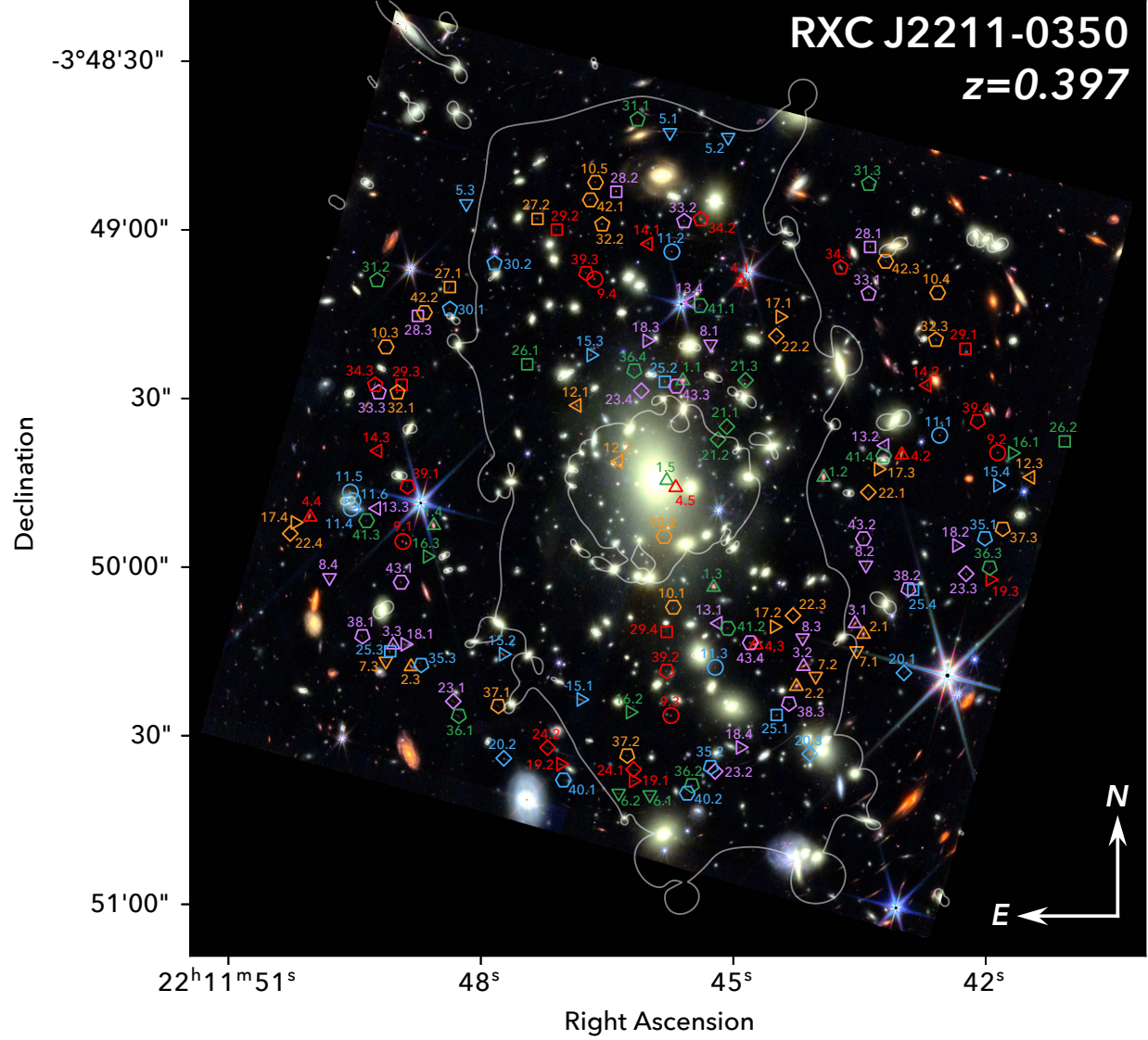


Figure S3: Multiple images used for the construction of the cluster mass models. Positions of 146 multiple images from 43 sources in RXC J2211–0350 are shown by symbols. In this Figure, ID 9 and 10 correspond to R2211-RX1 and R2211-RX2, respectively. White solid lines indicate critical curves of the best-fitting model for the source redshift of 4.3.

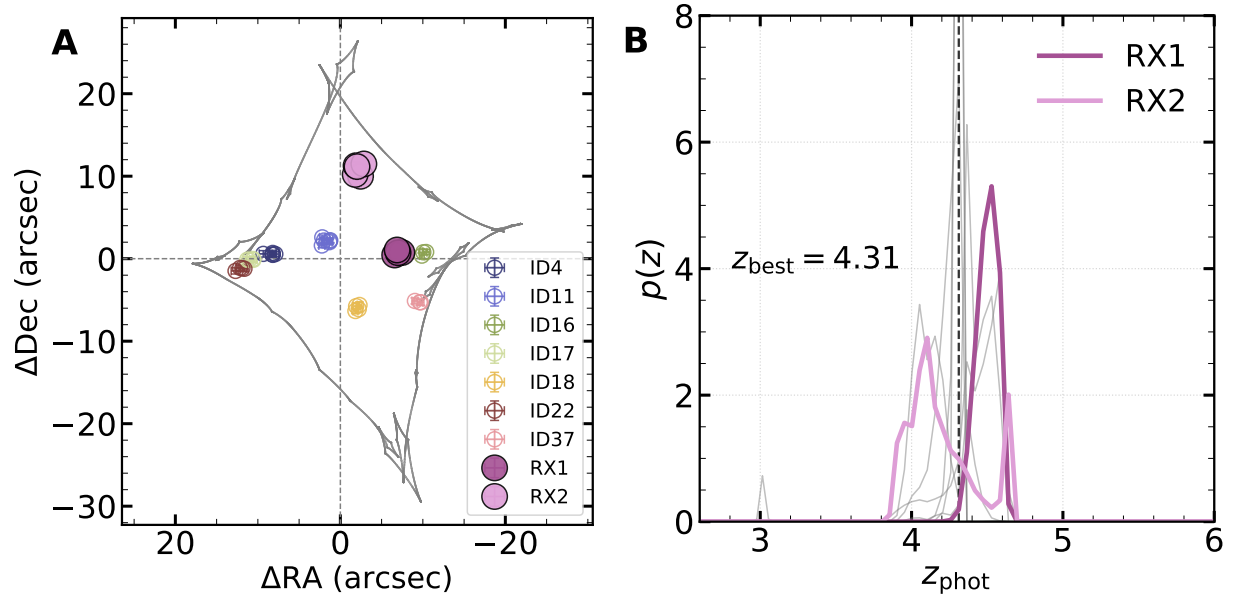


Figure S4: A potential overdensity of $z \sim 4.3$ galaxies including two LRDs. (A) Source-plane positions of multiply imaged sources with $z_{\text{phot}} \sim 4.3$ in RXC J2211–0350. The gray line represents the caustic curve for $z_s = 4.3$. (B) Photometric redshift distribution of sources in (A). The distribution of R2211-RX1 and R2211-RX2 are shown as purples, while other sources are shown as gray curves. The vertical dashed line $z_{\text{best}} = 4.31$ is the best z_{phot} jointly constrained by the z_{phot} distribution of other sources.

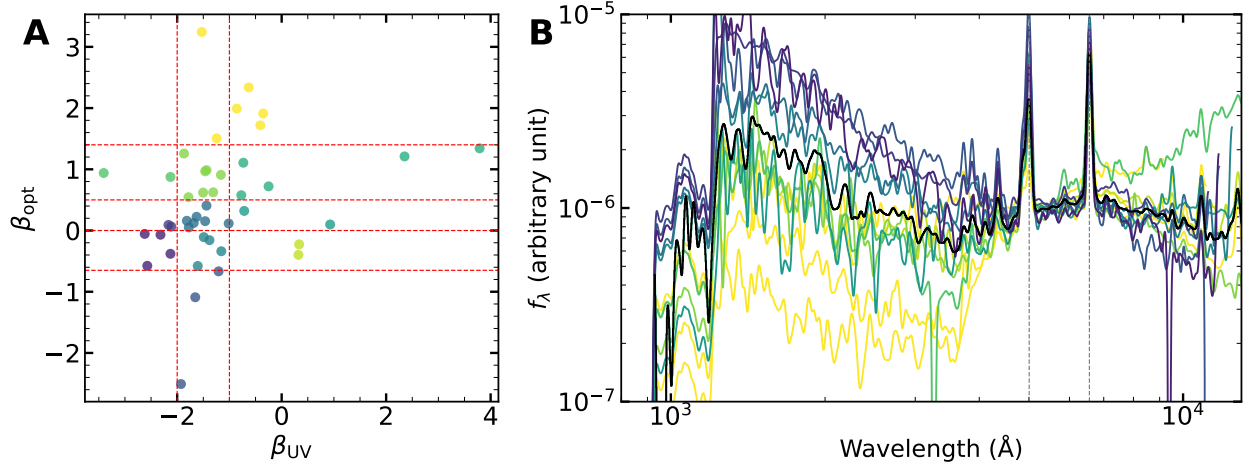


Figure S5: The construction of LRD spectral templates. (A) Distribution of LRDs used to construct z_{phot} fitting templates in the $(\beta_{UV}, \beta_{opt})$ plane, color-coded to be consistent with the stacked spectra in (B). The dashed red lines denote the adopted binning boundaries ($\beta_{UV} = -2.0, -1.0$; $\beta_{opt} = -0.65, 0.0, 0.5, 1.4$), which divide the sample into twelve subsamples with distinct UV-optical slopes. (B) Empirical rest-frame templates derived for each $(\beta_{UV}, \beta_{opt})$ bin (colored curves), ordered by their relative flux at 2000 \AA . The black curve shows the global median stack of all 44 LRDs. Vertical dashed lines mark the wavelengths of $[\text{O III}]$ and $\text{H}\alpha$ emission line. All spectra are normalized at 5500 \AA and smoothed with a Gaussian kernel with $\sigma = 5$.

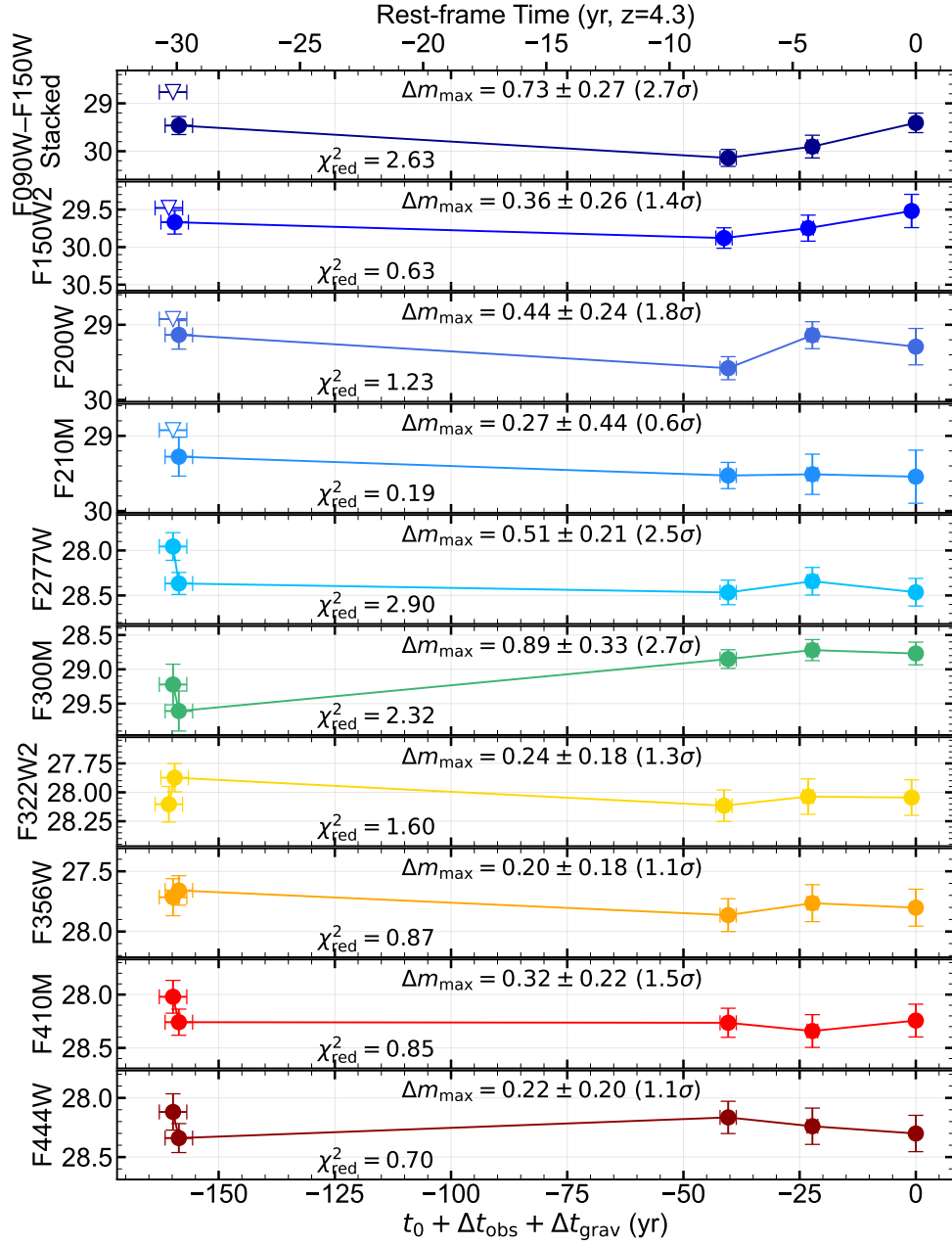


Figure S6: The same as Figure 2(A), but for R2211-RX2. Filled circles indicate detections, and open downward triangles represent 2σ upper limits.

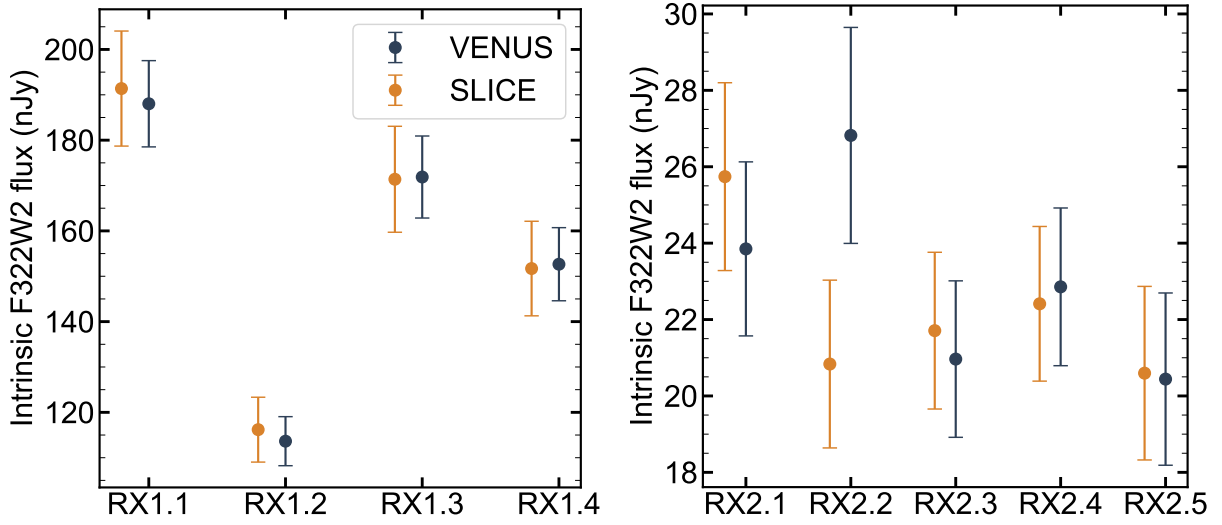


Figure S7: Comparison of intrinsic F322W2 fluxes from SLICE measurements and synthetic estimates derived from the mean of VENUS F277W and F356W measurements for R2211-RX1 and R2211-RX2. The error bars shown include both photometric uncertainties and magnification uncertainties. The rest-frame observation interval between SLICE and VENUS is ~ 0.2 yr. Overall, R2211-RX1 and R2211-RX2 do not show significant variability between the SLICE and VENUS observations (the difference for R2211-RX2.2 is $< 2\sigma$).

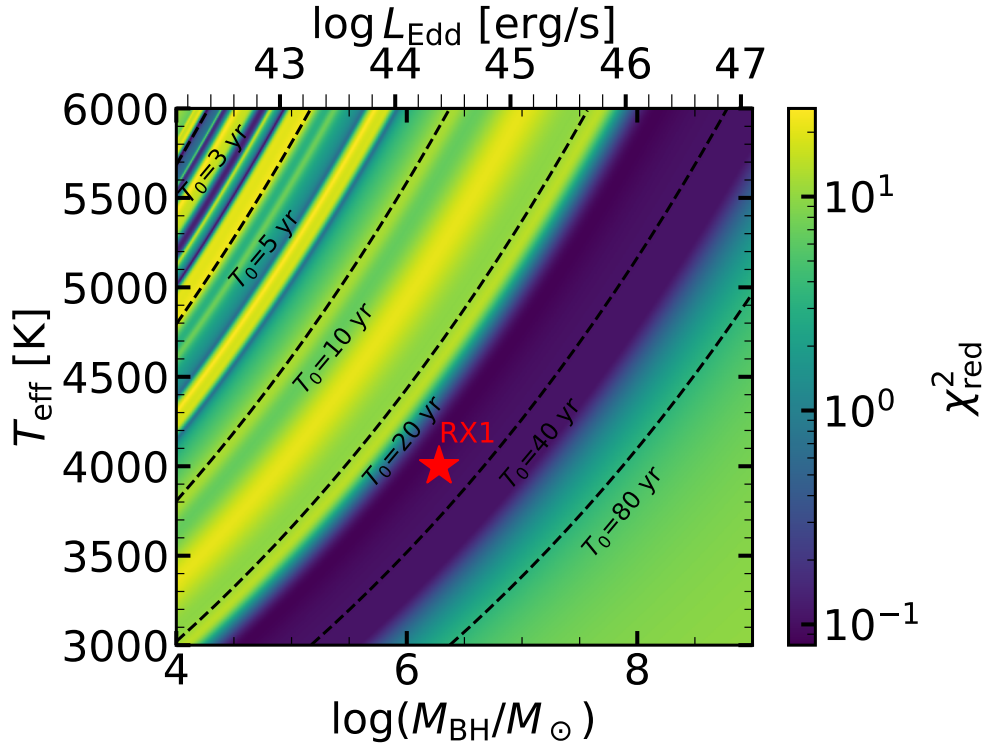


Figure S8: Total χ^2_v values of the light curves modeling over a grid of M_{BH} and T_{eff} . The color scale uses a logarithmic normalization to highlight the structure of the χ^2_v landscape. The red star marks the inferred properties of RX1 at $M_{\text{BH}} = 10^{6.28} M_{\odot}$ and $T_{\text{eff}} = 4000$ K. Black dashed lines show the loci of different characteristic pulsation periods $T_0 = 3, 5, 10, 20, 40,$ and 80 yr. The top x-axis indicates the corresponding $\log L_{\text{Edd}}$ for each M_{BH} .

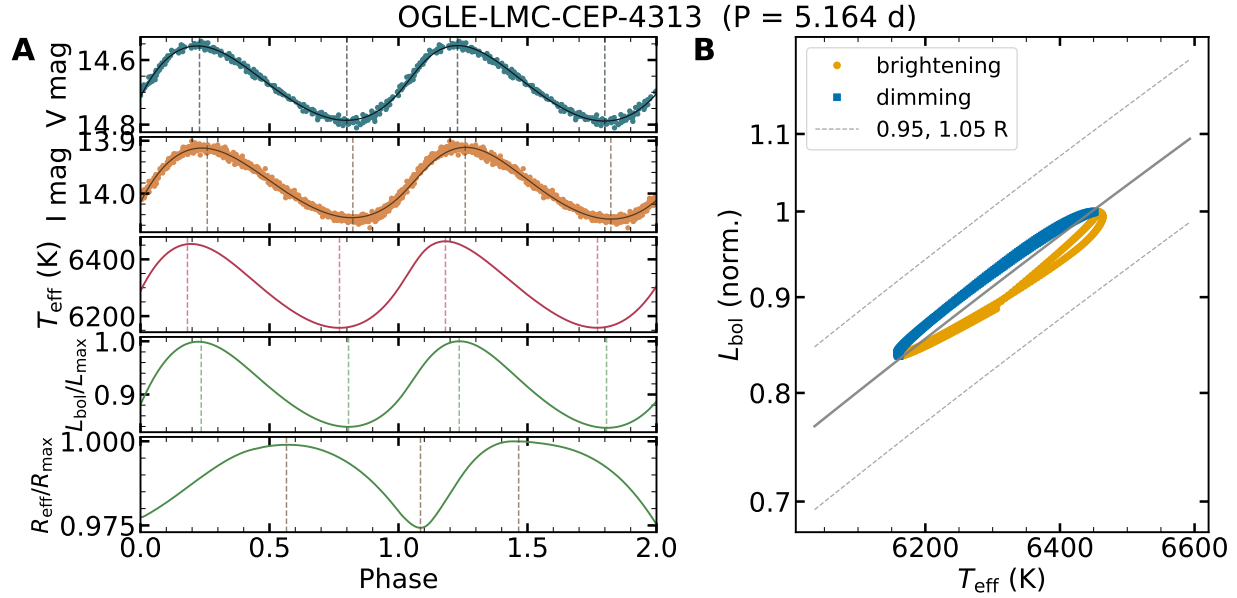


Figure S9: Multi-band light curves, temperature and luminosity evolution, and the corresponding HR loop for a Cepheid (OGLE-LMC-CEP-4313). (A) Phased V-band (top) and I-band (second panel) light curves, together with the best-fit spline models. Dashed vertical lines mark the phases of maximum and minimum brightness in each band. The third, fourth, and fifth panels show the inferred T_{eff} , L_{BB} , and R_{eff} as functions of phase, derived from the spline-interpolated V–I color using the YBC color-temperature and bolometric correction relations; their extrema are similarly indicated. (B) The resulting $T_{\text{eff}}-L_{\text{BB}}$ loop, separated into brightening (orange) and dimming (blue) branches. The loop illustrates the hysteresis between temperature and luminosity through the pulsation cycle. Gray curves denote constant mean radii and for radii offset by $\pm 5\%$ around the mean.

Table S2: List of multiple images used for strong lens mass modeling. The assumed positional error in units of arcsecond is indicated by σ_{pos} , and z and σ_z refer to the source redshift and its error, respectively. Photometric redshifts together with 1σ uncertainties are given with the absence of spectroscopic redshifts. If the redshift is not indicated, it is assumed to be a free parameter. ID 1, 2, and 3 are presented in (63), and ID 4, 5, 6, 7, 8, and 21 are presented in (29). ID 9 and 10 corresponds to R2211-RX1 and R2211-RX2, respectively. The spectroscopic redshifts of ID 14 and 32 are obtained through Keck/KCWI spectroscopy of $\text{Ly}\alpha$ emission (private communication).

ID	Redshift	RA [°]	Dec [°]	σ_{pos} ["]
1.1	1.051	332.94000	−3.82412	0.6
1.2		332.93302	−3.82889	0.6
1.3		332.93848	−3.83433	0.6
1.4		332.95233	−3.83127	0.6
1.5		332.94080	−3.82905	0.6
2.1	1.9±0.2	332.93105	−3.83665	0.6
2.2		332.93438	−3.83923	0.6
2.3		332.95345	−3.83825	0.6
3.1	2.0±0.2	332.93148	−3.83612	0.6
3.2		332.93403	−3.83824	0.6
3.3		332.95434	−3.83717	0.6
4.1	4.4±0.2	332.93711	−3.81924	0.6
4.2		332.92915	−3.82778	0.6
4.3		332.93637	−3.83717	0.6
4.4		332.95844	−3.83086	0.6

4.5		332.94035	−3.82940	0.6
5.1	...	332.94064	−3.81186	0.6
5.2		332.93776	−3.81210	0.6
5.3		332.95072	−3.81538	0.6
6.1	1.8±0.2	332.94164	−3.84459	0.6
6.2		332.94318	−3.84451	0.6
7.1	...	332.93139	−3.83747	0.6
7.2		332.93342	−3.83873	0.6
7.3		332.95470	−3.83799	0.6
8.1	3.2±0.2	332.93862	−3.82232	0.6
8.2		332.93094	−3.83324	0.6
8.3		332.93407	−3.83684	0.6
8.4		332.95750	−3.83386	0.6
9.1	4.3±0.4	332.95386	−3.83207	0.6
9.2		332.92441	−3.82768	0.6
9.3		332.94059	−3.84067	0.6
9.4		332.94436	−3.81911	0.6
10.1	4.3±0.4	332.94047	−3.83532	0.6
10.2		332.94092	−3.83182	0.6
10.3		332.95469	−3.82245	0.6
10.4		332.92738	−3.81977	0.6
10.5		332.94432	−3.81432	0.6
11.1	4.3±0.4	332.92728	−3.82682	0.6
11.2		332.94054	−3.81775	0.6
11.3		332.93839	−3.83829	0.6
11.4		332.95642	−3.83043	0.2
11.5		332.95646	−3.82963	0.2
11.6		332.95633	−3.83006	0.2
12.1	2.6±0.2	332.94524	−3.82534	0.6
12.2		332.94318	−3.82812	0.6

12.3		332.92278	−3.82890	0.6
13.1	1.8±0.2	332.93826	−3.83611	0.6
13.2		332.93000	−3.82732	0.6
13.3		332.95517	−3.83043	0.6
13.4		332.93961	−3.82022	0.6
14.1	2.535	332.94171	−3.81736	0.6
14.2		332.92791	−3.82434	0.6
14.3		332.95511	−3.82759	0.6
15.1	2.4±0.2	332.94504	−3.83988	0.6
15.2		332.94888	−3.83764	0.6
15.3		332.94454	−3.82286	0.6
15.4		332.92441	−3.82929	0.6
16.1	4.4±0.2	332.92367	−3.82770	0.6
16.2		332.94260	−3.84050	0.6
16.3		332.95265	−3.83281	0.6
17.1	4.4±0.2	332.93518	−3.82096	0.6
17.2		332.93546	−3.83628	0.6
17.3		332.93031	−3.82849	0.6
17.4		332.95919	−3.83113	0.6
18.1	4.0±0.2	332.95375	−3.83715	0.6
18.2		332.92643	−3.83227	0.6
18.3		332.94177	−3.82215	0.6
18.4		332.93715	−3.84224	0.6
19.1	3.6±0.2	332.94244	−3.84389	0.6
19.2		332.94604	−3.84307	0.6
19.3		332.92478	−3.83394	0.6
20.1	2.3±0.2	332.92905	−3.83857	0.6
20.2		332.94886	−3.84278	0.6
20.3		332.93371	−3.84257	0.6
21.1	6.4±0.2	332.93782	−3.82639	0.2

21.2		332.93826	-3.82703	0.2
21.3		332.93689	-3.82410	0.6
22.1	4.4±0.2	332.93081	-3.82963	0.6
22.2		332.93537	-3.82191	0.6
22.3		332.93454	-3.83573	0.6
22.4		332.95944	-3.83167	0.6
23.1	3.5±0.2	332.95137	-3.83997	0.6
23.2		332.93840	-3.84343	0.6
23.3		332.92597	-3.83366	0.6
23.4		332.94205	-3.82462	0.6
24.1	3.2±0.2	332.94244	-3.84333	0.6
24.2		332.94670	-3.84226	0.6
25.1	3.0±0.2	332.93535	-3.84064	0.6
25.2		332.94089	-3.82417	0.6
25.3		332.95449	-3.83749	0.6
25.4		332.92860	-3.83446	0.6
26.1	6.4±0.2	332.94770	-3.82331	0.6
26.2		332.92109	-3.82712	0.6
27.1	2.0±0.2	332.95153	-3.81949	0.6
27.2		332.94719	-3.81613	0.6
28.1	3.1±0.2	332.93073	-3.81751	0.6
28.2		332.94329	-3.81478	0.6
28.3		332.95312	-3.82092	0.6
29.1	3.6±0.2	332.92601	-3.82254	0.6
29.2		332.94624	-3.81665	0.6
29.3		332.95392	-3.82433	0.6
29.4		332.94080	-3.83653	0.0
30.1	3.3±0.5	332.95153	-3.82058	0.6
30.2		332.94932	-3.81832	0.6

31.1	7.3±0.2	332.94224	−3.81121	0.6
31.2		332.95513	−3.81916	0.6
31.3		332.93079	−3.81439	0.6
32.1	2.647	332.95413	−3.82471	0.6
32.2		332.94399	−3.81640	0.6
32.3		332.92747	−3.82210	0.6
33.1	2.2±0.2	332.93080	−3.81982	0.6
33.2		332.93993	−3.81624	0.6
33.3		332.95506	−3.82470	0.6
34.1	2.2±0.2	332.93218	−3.81853	0.6
34.2		332.93911	−3.81615	0.6
34.3		332.95523	−3.82433	0.6
35.1	6.4±0.2	332.92504	−3.83190	0.6
35.2		332.93862	−3.84321	0.6
35.3		332.95295	−3.83817	0.6
36.1	5.7±0.2	332.95109	−3.84068	0.6
36.2		332.93955	−3.84412	0.6
36.3		332.92481	−3.83336	0.6
36.4		332.94240	−3.82362	0.6
37.1	4.2±0.2	332.94913	−3.84019	0.6
37.2		332.94275	−3.84264	0.6
37.3		332.92416	−3.83144	0.6
38.1	3.9±0.2	332.95586	−3.83674	0.6
38.2		332.92883	−3.83442	0.6
38.3		332.93474	−3.84008	0.6
39.1	3.2±0.2	332.95363	−3.82934	0.6
39.2		332.94080	−3.83846	0.6
39.3		332.94479	−3.81880	0.6
39.4		332.92541	−3.82612	0.6

40.1	2.3±0.2	332.94591	−3.84386	0.6
40.2		332.93978	−3.84451	0.6
41.1	2.1±0.2	332.93915	−3.82041	0.6
41.2		332.93777	−3.83636	0.6
41.3		332.95566	−3.83104	0.6
41.4		332.93005	−3.82783	0.6
42.1	2.0±0.5	332.94458	−3.81519	0.6
42.2		332.95279	−3.82075	0.6
42.3		332.92995	−3.81822	0.6
43.1	...	332.95395	−3.83408	0.6
43.2		332.93106	−3.83193	0.6
43.3		332.94032	−3.82439	0.6
43.4		332.93666	−3.83707	0.6